Received: 7 August 2021 | Revised: 14 February 2022 | Accepted: 14 February 2022

DOI: 10.1002/nme.7010

RESEARCH ARTICLE

WILEY

Vibration analysis of piezoelectric Kirchhoff–Love shells based on Catmull–Clark subdivision surfaces

Zhaowei Liu[1,2] | **Andrew McBride**[2] | **Prashant Saxena**[2] | **Luca Heltai**[3] | **Yilin Qu**[4] | **Paul Steinmann**[2,5]

[1]College of Mechanics and Materials, Hohai University, Nanjing, China

[2]Glasgow Computational Engineering Centre, University of Glasgow, Glasgow, United Kingdom

[3]SISSA (International School for Advanced Studies), Trieste, Italy

[4]State Key Laboratory for Strength and Vibration of Mechanical Structures, Xi'an Jiaotong University, Xi'an, Shaanxi, China

[5]Institute of Applied Mechanics, Friedrich-Alexander Universität Erlangen-Nürnberg, Erlangen, Germany

Correspondence
Zhaowei Liu, College of Mechanics and Materials, Hohai University, Nanjing 211100, China
Email: zhaowei.liu@hhu.edu.cn

Funding information
Central University Basic Research Fund of China, Grant/Award Number: xzy022020016; Deutsche Forschungsgemeinschaft, Grant/Award Number: GRK2495 B&C; Engineering and Physical Sciences Research Council, Grant/Award Number: EP/R008531/1

Abstract

An isogeometric Galerkin approach for analysing the free vibrations of piezoelectric shells is presented. The shell kinematics is specialized to infinitesimal deformations and follow the Kirchhoff–Love hypothesis. Both the geometry and physical fields are discretized using Catmull–Clark subdivision bases. This provides the required C^1-continuous discretization for the Kirchhoff–Love theory. The crystalline structure of piezoelectric materials is described using an anisotropic constitutive relation. Hamilton's variational principle is applied to the dynamic analysis to derive the weak form of the governing equations. The coupled eigenvalue problem is formulated by considering the problem of harmonic vibration in the absence of external load. The formulation for the purely elastic case is verified using a spherical thin shell benchmark. Thereafter, the piezoelectric shell formulation is verified using a one dimensional piezoelectric beam. The piezoelectric effect and vibration modes of a transverse isotropic curved plate are analyzed and evaluated for the Scordelis–Lo roof problem. Finally, the eigenvalue analysis of a CAD model of a piezoelectric speaker shell structure showcases the ability of the proposed method to handle complex geometries.

KEYWORDS

Catmull–Clark subdivision surfaces, eigenvalue analysis, isogeometric analysis, Kirchhoff–Love shell, piezoelectricity

1 | INTRODUCTION

Piezoelectricity is a reversible two-way coupling effect resulting from electromechanical interactions in certain crystalline materials. In 1880, Curie and Curie[1] discovered the direct piezoelectric effect whereby a mechanical excitation generates an electrical potential. Shortly thereafter, Lippmann[2] derived the converse piezoelectric effect from fundamental thermodynamic principles. In 1881, Curie and Curie[3] proved the existence of a strain that occurs when an electric field is applied. Shortly after the piezoelectric phenomenon was discovered, Langevin and Rutherford independently applied the piezoelectric effect for submarine detection.[4] In the last century the piezoelectric effect has been extensively studied. A wide

range of novel piezoelectric materials have been developed and the resulting devices applied to engineering applications. The direct piezoelectric effect is used in sensors/transducers[5-10] and energy harvesters,[11,12] and the converse piezoelectric effect is used in resonators[13-15] and actuators.[16-18]

Piezoelectric sensors and actuators are often constructed from films, plates and shells as they can generate large strains under small loads. Early studies of piezoelectric structures focused on simple geometries such as rods,[19] plates,[20,21] and cylindrical shells.[22,23] Laminated piezoelectric plates[24,25] are also well studied. With the development of active, adaptive and smart structures, piezoelectric materials are now widely used because of their ability to achieve a precise and complex mechanical response to electrical loads. This motivates the requirement for analysis of piezoelectric structures with complex geometries. The finite element method is the ideal modeling framework to analyse such complex structures and to deal with the inherent nonlinearities. Allik and Hughes[26] proposed a three-dimensional finite element method for electroelastic analyses, focussing mainly on piezoelectric vibrations. The early works of the piezoelectric finite element method have been reviewed by Benjeddou.[27] Tzou and Tseng[8] evaluated the performance of intelligent piezoelectric thin plates using a finite element approach. Hwang and Park[18] developed a finite element model of laminated plates with piezoelectric sensors and actuators. A nonlinear finite element approach to phase transition in piezoelectric materials was proposed by Ghandi and Hagoo,[28] while Lam et al.[29] analysed piezoelectric composite laminates. A static and dynamic analysis of a piezoelectric bimorph was undertaken by Wang.[30]

Although many three-dimensional finite element approaches for piezoelectric structures have been proposed, work on piezoelectric Kirchhoff–Love shells is limited. Kirchhoff–Love and Reissner–Mindlin shell theories categorize shells into "thin" and "thick" according to the ratio of curvature radius to thickness. The Kirchhoff–Love shell theory, also called the "classical shell model", is tailored to thin shells. The Reissner–Mindlin shell theory is an extension of the Kirchhoff–Love theory, which can be applied to both thin and thick shells since it accounts for shear deformations. However, Reissner–Mindlin shells theory requires additional rotational degrees of freedom, resulting in a larger system matrix than the Kirchhoff–Love shell theory. Kirchhoff–Love shells require only three translational degrees of freedom, which is computationally more efficient. However, the Kirchhoff–Love finite element method requires C^1-continuity of the basis functions while a conventional Lagrangian interpolation only provides C^0-continuity.

Hughes et al.[31] presented the framework for isogeometric analysis (IGA) in 2005. IGA provides higher-order continuity by using splines as interpolation functions and thereby allows for exact geometric representation which completely eliminates geometry error in the numerical solution. However, volume parameterization of a computer aided desgin (CAD) model is the most challenging problem for IGA.[32] Shell formulations are well suited for IGA since they only require a discretization of the mid-surfaces of the shell. Kiendl et al.[33] developed an isogeometric approach for Kirchhoff–Love shells using non-uniform rational B-splines (NURBS). Isogeometric Reissner–Mindlin shells have also been extensively studied in References 34 and 35. Cirak et al.[36] developed a C^1-conforming discretization based on Loop subdivision surfaces for an elastic Kirchhoff–Love shell formulation and applied it to hyperelastic thin shells.[37] Subdivision surfaces are an alternative to NURBS surfaces. They represent a mature geometry modeling method that is widely used in the animation and gaming industry, and is also widely available in CAD packages. An attractive feature of subdivision surfaces is that they can be evaluated using spline functions, while retaining a simple polygonal mesh data structure able to represent complex geometries. Extraordinary vertices in the mesh allow for local refinement and patch conforming, both challenges faced by NURBS. Subdivision surfaces shell formulations have been extended to applications including shell fracture,[38] shape optimization,[39,40] fluid-structure interaction,[41] nonmanifold geometry[42] and structural-acoustic analysis.[43] The ability of subdivision surfaces to analyse thin shells underpins the analysis of the electromechanical coupled thin shells presented here.

Applications for piezoelectric shells, such as resonators, actuators and energy harvesters, often involve the structural dynamics. Thus, understanding the effect of electroelastic coupling on the vibration mode of piezoelectric structures is critical. The coupling effect will influence the lattice structure of the piezoelectric material and enhance the stiffness of such structure via the so-called "piezoelectric stiffening" effect.[44] Thus, the natural frequencies of vibration modes increase. This effect is used in laminated beams[45] and plates[46] with piezoelectric actuators to enhance their stiffness. However, the "piezoelectric stiffening" effect of piezoelectric thin shells with complex geometry is seldom studied. This work provides a numerical analysis tool for understanding these effects in piezoelectric thin shells.

The proposed method adopts Catmull–Clark subdivision surfaces to formulate a novel isogeometric Galerkin approach to analyse piezoelectric thin shells with arbitrary geometries. The formulation for analysing piezoelectric thin shells is carefully presented. Physically meaningful electric conditions are considered, these are no electrodes, prescribed voltage with electrodes and short-circuited electrodes. A potential application of our new formulation is demonstrated

via a method to tailor the natural frequency of a piezoelectric curved plate by changing its curvature. In addition, the proposed method also provides, for the first time, a way to examine the "piezoelectric stiffening" effect of piezoelectric thin shells with complex geometry.

This contribution is organized as follows. Section 2 introduces the notation and defines various coordinate systems used throughout the manuscript. Section 3 illustrates the kinematics of Kirchhoff–Love shells. Section 4 briefly reiterates the theory of Catmull–Clark subdivision surfaces. A detailed formulation of our new isogeometric Galerkin approach for piezoelectric shells is presented in Section 5. Finally, Section 6 presents four numerical examples to demonstrate the ability of the proposed piezoelectric thin shell method to deal with various geometries and a range of mechanical and coupled problems.

2 | NOTATION

Brackets:
Two types of brackets are used. Square brackets [] are used to clarify the order of operations in an algebraic expression. Circular brackets () are used to denote the parameters of a function. If brackets are used to denote an interval then () stands for an open interval and [] is a closed interval.

Symbols:
A variable typeset in a normal weight font represents a scalar. A bold weight font denotes a tensor. An overline indicates that the variable is defined with respect to the reference configuration and if absent, the variable is defined with respect to the current (deformed) configuration. A scalar variable with superscript or subscript indices normally represents the components of a vector or tensor. Upright font is used to denote matrices and vectors.

Indices $i, j, k, \ldots$ vary from 1 to 3 while $a, b, c, \ldots$, used as surface variable components, vary from 1 to 2. Einstein summation convention is used throughout.

The comma symbol in a subscript represents partial derivative, for example, $A_{,b}$ is the partial derivative of A with respect to its bth component. $\nabla(\bullet)$ is the three-dimensional gradient operator.

Coordinates:
$\mathbf{c}_i$ represent the basis vectors of an orthonormal system in three-dimensional Euclidean space and x, y, and z are its components. $\boldsymbol{\xi}_i$ denote the orthonormal basis vectors in the local element space and ξ, η, and ζ are its coordinate components. The three covariant basis vectors for a surface point are denoted as $\mathbf{a}_i$, where $\mathbf{a}_1, \mathbf{a}_2$ are two tangential vectors and $\mathbf{a}_3$ is the normal vector.

3 | KIRCHHOFF–LOVE SHELL KINEMATICS

The Kirchhoff–Love hypothesis can be applied to three-dimensional structures in which one dimension is much smaller than the other two. Important examples include plates and shells. It is assumed that lines perpendicular to the mid-surface remain straight and perpendicular to the mid-surface after deformation (see Figure 1). The shell occupies the physical domain Ω and has a uniform thickness h. Figure 2 shows the reference and deformed configurations of the mid-surface. The shell kinematics are restricted to infinitesimal deformations, and hence the thickness does not change upon deformation. The mid-surface of the shell in both the reference and deformed configurations is denoted by Γ. Points on the mid-surface in the reference and the deformed configurations are denoted by $\bar{\mathbf{x}}$ and $\mathbf{x}$, respectively, and are obtained as map from the parametric coordinates ξ and η. The position vector of a point in the deformed configuration $\mathbf{r}$ is computed using the mid-surface point $\mathbf{x}$ and the normal vector $\mathbf{n}$ as

$$\mathbf{r}(\xi, \eta, \zeta) = \mathbf{x}(\xi, \eta) + \zeta \mathbf{n}(\xi, \eta), \tag{1}$$

where $\zeta \in [-h/2, h/2]$. A mid-surface point in the deformed configuration $\mathbf{x}$ can be expressed as

$$\mathbf{x} = \bar{\mathbf{x}} + \mathbf{u}, \tag{2}$$

where $\mathbf{u}$ denotes the displacement.

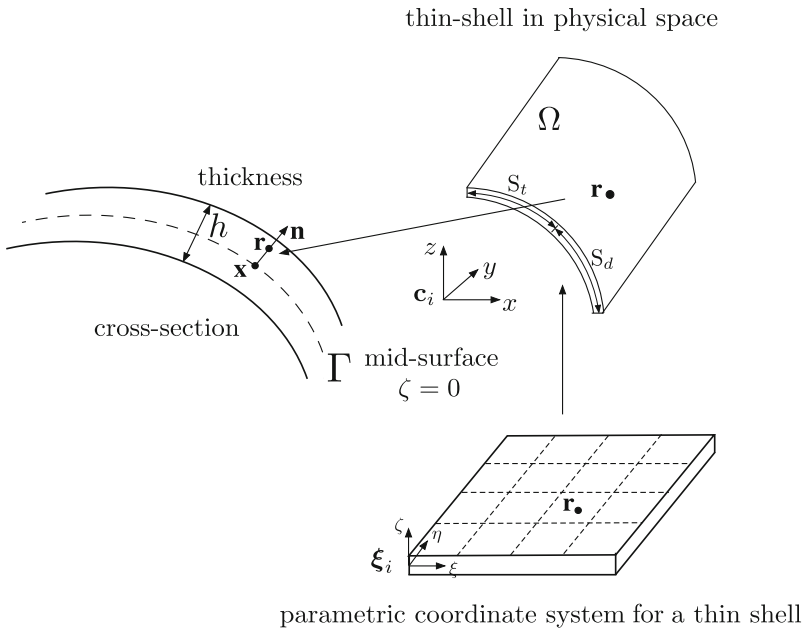

FIGURE 1 Kirchhoff–Love shell of thickness h occupying region Ω and mid-surface Γ is parametrized by the coordinate system (ξ, η, ζ).

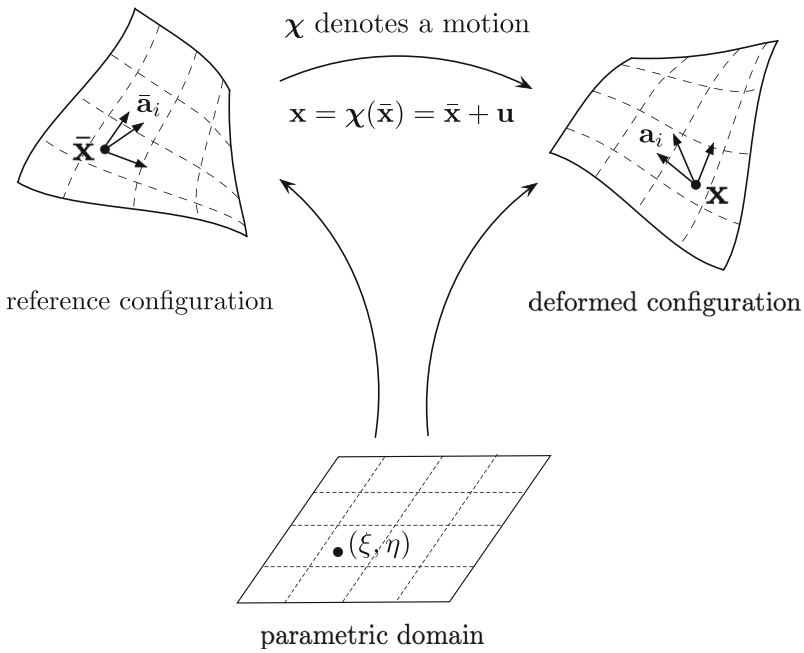

FIGURE 2 Reference and deformed configurations for the mid-surface of a Kirchhoff–Love shell

3.1 | Green–Lagrangian strain tensor

The covariant basis vectors of the tangent plane of the mid-surface in the reference and the deformed configurations are defined by

$$\bar{\mathbf{a}}_1 = \frac{\partial \bar{\mathbf{x}}}{\partial \xi}, \quad \bar{\mathbf{a}}_2 = \frac{\partial \bar{\mathbf{x}}}{\partial \eta} \quad \text{and} \quad \mathbf{a}_1 = \frac{\partial \mathbf{x}}{\partial \xi}, \quad \mathbf{a}_2 = \frac{\partial \mathbf{x}}{\partial \eta}. \tag{3}$$

Thus, the normal vectors in the two configurations can be computed as

$$\bar{\mathbf{n}} = \bar{\mathbf{a}}_3 = \frac{\bar{\mathbf{a}}_1 \times \bar{\mathbf{a}}_2}{\bar{J}} \quad \text{and} \quad \mathbf{n} = \mathbf{a}_3 = \frac{\mathbf{a}_1 \times \mathbf{a}_2}{J}, \tag{4}$$

where $\bar{J}$ and J are the respective Jacobians given by

$$\bar{J} = |\bar{\mathbf{a}}_1 \times \bar{\mathbf{a}}_2| \quad \text{and} \quad J = |\mathbf{a}_1 \times \mathbf{a}_2|. \tag{5}$$

Thus, the covariant components of the metric tensor for the mid-surface points $\bar{\mathbf{x}}$ and $\mathbf{x}$ are respectively given by

$$\bar{a}_{ij} = \bar{\mathbf{a}}_i \cdot \bar{\mathbf{a}}_j \quad \text{and} \quad a_{ij} = \mathbf{a}_i \cdot \mathbf{a}_j. \tag{6}$$

The contravariant metric tensors are defined by

$$\bar{a}^{ik}\bar{a}_{kj} = \delta^i_j \quad \text{and} \quad a^{ik}a_{kj} = \delta^i_j, \tag{7}$$

where δ^i_j denotes the Kronecker delta. The three-dimensional covariant basis vectors for the shell in the reference and the deformed configurations are respectively given by

$$\bar{\mathbf{g}}_1 = \frac{\partial \bar{\mathbf{r}}}{\partial \xi} = \bar{\mathbf{a}}_1 + \zeta \bar{\mathbf{a}}_{3,1}, \quad \bar{\mathbf{g}}_2 = \frac{\partial \bar{\mathbf{r}}}{\partial \eta} = \bar{\mathbf{a}}_2 + \zeta \bar{\mathbf{a}}_{3,2}, \quad \bar{\mathbf{g}}_3 = \frac{\partial \bar{\mathbf{r}}}{\partial \zeta} = \bar{\mathbf{a}}_3, \tag{8}$$

and

$$\mathbf{g}_1 = \frac{\partial \mathbf{r}}{\partial \xi} = \mathbf{a}_1 + \zeta \mathbf{a}_{3,1}, \quad \mathbf{g}_2 = \frac{\partial \mathbf{r}}{\partial \eta} = \mathbf{a}_2 + \zeta \mathbf{a}_{3,2}, \quad \mathbf{g}_3 = \frac{\partial \mathbf{r}}{\partial \zeta} = \mathbf{a}_3, \tag{9}$$

where $(\bullet)_{,1}$ and $(\bullet)_{,2}$ represent the partial differentials with respect to ξ and η, respectively. The components of the covariant metric tensors are defined by

$$\bar{g}_{ij} = \bar{\mathbf{g}}_i \cdot \bar{\mathbf{g}}_j \quad \text{and} \quad g_{ij} = \mathbf{g}_i \cdot \mathbf{g}_j, \tag{10}$$

which allows one to define the Green–Lagrange strain tensor $\mathbf{S}_n$ as

$$\mathbf{S}_n := \frac{1}{2}[g_{ij} - \bar{g}_{ij}]\bar{\mathbf{g}}^i \otimes \bar{\mathbf{g}}^j, \tag{11}$$

where $\bar{\mathbf{g}}^i$ denote the contravariant basis vectors defined by

$$\bar{\mathbf{g}}^i \cdot \bar{\mathbf{g}}_j = \delta^i_j. \tag{12}$$

3.2 | Linearization and simplification of the strain tensor

On substituting Equations (8) and (9) into (11) and ignoring higher-order terms, the Green–Lagrange strain tensor linearized in ζ follows as

$$\mathbf{S} = \mathbf{A} + \zeta \mathbf{B}. \tag{13}$$

The components of the tensors $\mathbf{A}$ and $\mathbf{B}$ are α_{ij} and β_{ij}, respectively, with α_{13} and α_{23} measuring the shearing in the normal direction $\bar{\mathbf{a}}_3$, and which are zero under the Kirchhoff–Love assumption. The stretching in normal direction is given by $\alpha_{33} = 0$ and vanishes due to the assumption that the thickness does not change with deformation. Similarly, $\beta_{i3} = 0$ as the

normal vector is perpendicular to the two basis vectors. Thus, the two tensors **A** and **B** reduce to two-dimensional tensors in the subspace defined with two contravariant basis vectors as

$$\mathbf{A} := \alpha_{ab}\, \bar{\mathbf{g}}^a \otimes \bar{\mathbf{g}}^b \quad \text{and} \quad \mathbf{B} := \beta_{ab}\, \bar{\mathbf{g}}^a \otimes \bar{\mathbf{g}}^b, \tag{14}$$

where their components are computed as

$$\alpha_{ab} = \frac{1}{2}[\mathbf{a}_a \cdot \mathbf{a}_b - \bar{\mathbf{a}}_a \cdot \bar{\mathbf{a}}_b] \quad \text{and} \quad \beta_{ab} = \mathbf{a}_a \cdot \mathbf{a}_{3,b} - \bar{\mathbf{a}}_a \cdot \bar{\mathbf{a}}_{3,b}. \tag{15}$$

The membrane strain components are denoted as α_{ab} while the bending strain components β_{ab} measure the change in the curvature of the shell. In order to compute the bending strain tensor, the product rule of differentiation is applied and the components expressed as

$$\beta_{ab} = \bar{\mathbf{a}}_{a,b} \cdot \bar{\mathbf{a}}_3 - \mathbf{a}_{a,b} \cdot \mathbf{a}_3. \tag{16}$$

On substituting Equation (2) into the membrane and bending strains, the components can eventually be computed to first order in **u** as

$$\alpha_{ab} = \frac{1}{2}[\bar{\mathbf{a}}_a \cdot \mathbf{u}_{,b} + \mathbf{u}_{,a} \cdot \bar{\mathbf{a}}_b], \tag{17}$$

$$\beta_{ab} = -\mathbf{u}_{,ab} \cdot \bar{\mathbf{a}}_3 + \frac{1}{\bar{J}}\left[\mathbf{u}_{,1} \cdot [\bar{\mathbf{a}}_{a,b} \times \bar{\mathbf{a}}_2] + \mathbf{u}_{,2} \cdot [\bar{\mathbf{a}}_1 \times \bar{\mathbf{a}}_{a,b}]\right] + \frac{\bar{\mathbf{a}}_3 \cdot \bar{\mathbf{a}}_{a,b}}{\bar{J}}\left[\mathbf{u}_{,1} \cdot [\bar{\mathbf{a}}_2 \times \bar{\mathbf{a}}_3] + \mathbf{u}_{,2} \cdot [\bar{\mathbf{a}}_3 \times \bar{\mathbf{a}}_1]\right]. \tag{18}$$

Thus, the linearized strain tensor **S** is computed using the covariant basis vectors along with the first and second derivatives of the displacement **u**.

4 | CATMULL–CLARK SUBDIVISION SURFACES

Kirchhoff–Love shells require that the test and trial functions of the Galerkin method are in the Hilbert space $H^2(\Omega)$.[36] Hence a C^1-continuous discretization is required. Conventional Lagrangian bases only provide C^0-continuity. Catmull–Clark subdivision surfaces,[47] which adopt cubic B-splines as interpolating functions, display C^2 continuity everywhere except at the surface points related to extraordinary vertices,[48] where continuity is only C^1. Figure 3 shows an example of cubic B-splines for one dimensional elements. The Catmull–Clark subdivision surfaces adopt a tensor-product structure of two cubic B-splines to interpolate points on a two-dimensional surface. Figure 4 shows a smooth surface constructed by successive subdivision from a coarse polygonal mesh using the Catmull–Clark subdivision scheme.[49] The surface, composed of points $\bar{\mathbf{x}} \in \Gamma$, can be interpolated using the basis functions (cubic B-splines) and control points as

$$\bar{\mathbf{x}} = \sum_{A=0}^{n_b-1} N^A \mathbf{P}_A, \tag{19}$$

where n_b is the number of basis functions. The Ath basis function is denoted as N^A and $\mathbf{P}_A$ denotes the Ath control point. An element of a regular patch with 16 basis functions is shown in Figure 4. We note that the control points are not necessarily on the surface Γ. It is well known that the Galerkin method with Catmull–Clark subdivision surfaces can exhibit suboptimal convergence rate.[50]

5 | PIEZOELECTRIC SHELL FORMULATION

The energy considerations required for piezoelectric thin shells are presented first. Hamilton's variational principle is then applied and the resulting weak form of the governing equations of piezoelectric shells are derived. Finally, the weak

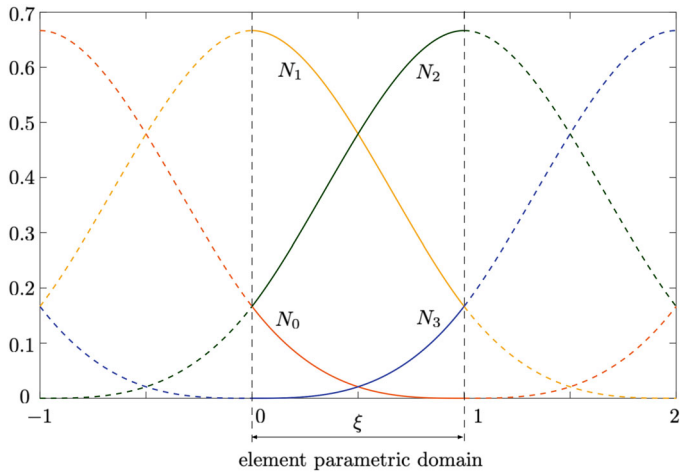

FIGURE 3 An example of cubic B-splines in a one-dimensional parametric domain. Spline functions span multiple elements.

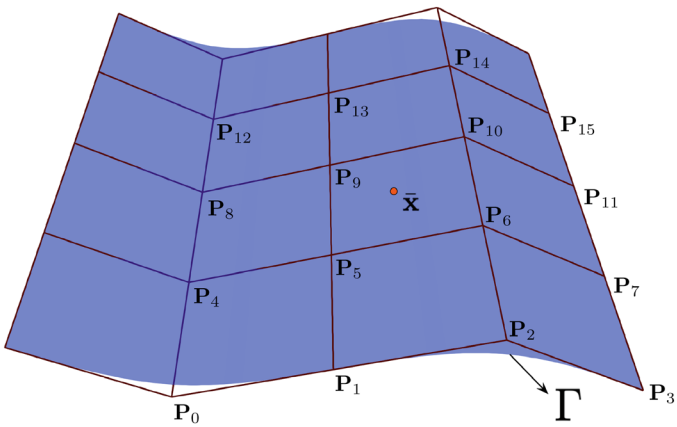

FIGURE 4 The mid-surface of the shell Γ is a Catmull–Clark subdivision surface constructed from a control polygonal mesh.

form of the governing equations is discretized using Catmull–Clark subdivision bases resulting in the discrete system of equations.

5.1 | Energy densities

The electric enthalpy density per unit volume for a coupled piezoelectric problem[51,52] is most generally defined by

$$\mathcal{H}(\mathbf{S},\mathbf{E}) = W_{\text{ela}}(\mathbf{S}) - W_{\text{piezo}}(\mathbf{S},\mathbf{E}) - W_{\text{elec}}(\mathbf{E}). \tag{20}$$

The electric enthalpy density contains the elastic energy density W_{ela}, the piezoelectric energy density W_{piezo} and the electric energy density W_{elec}. The electric field is denoted as $\mathbf{E}$. The piezoelectric and electric energy densities are expressed as

$$W_{\text{piezo}}(\mathbf{S},\mathbf{E}) = \mathbf{E}\cdot[\mathbf{e} : \mathbf{S}] = e^{ijk}E_i[\alpha_{jk} + \zeta\beta_{jk}], \tag{21}$$

and

$$W_{\text{elec}}(\mathbf{E}) = \frac{1}{2}[\boldsymbol{\kappa}\cdot\mathbf{E}]\cdot\mathbf{E} = \frac{1}{2}\kappa^{ij}E_iE_j, \tag{22}$$

respectively. The components of the third-order piezoelectric tensor $\mathbf{e}$ are e^{ijk} while κ^{ij} are the components of the second-order dielectric tensor $\boldsymbol{\kappa}$. Since the structure is thin and has uniform thickness, we introduce the quadratic elastic strain energy density per unit area $\tilde{W}_{\text{ela}}$ for the Kirchhoff–Love shell as

$$\tilde{W}_{\text{ela}}(\mathbf{S}) = \int_{-\frac{h}{2}}^{\frac{h}{2}} W_{\text{ela}}(\mathbf{S})\, \mathrm{d}\zeta. \tag{23}$$

A piezoelectric material is normally anisotropic due to the interaction between the mechanical and electrical states in crystalline materials with no inversion symmetry. Thus, with $\mathbf{S} = \mathbf{A} + \zeta\mathbf{B}$, one defines a general formulation for the elastic energy density per unit area by

$$\tilde{W}_{\text{ela}}(\mathbf{S}) = \tilde{W}_{\text{ela}}(\mathbf{A}, \mathbf{B}) = \frac{h}{2}\left[[\mathbf{A} : \mathbf{C} : \mathbf{A}] + \frac{h^2}{12}[\mathbf{B} : \mathbf{C} : \mathbf{B}]\right], \tag{24}$$

where $\mathbf{C}$ is the fourth-order elastic tensor which can be defined using the covariant base vectors by

$$\mathbf{C} = C^{ijkl}\bar{\mathbf{g}}_i \otimes \bar{\mathbf{g}}_j \otimes \bar{\mathbf{g}}_k \otimes \bar{\mathbf{g}}_l = \tilde{C}^{mnop}\mathbf{t}_m \otimes \mathbf{t}_n \otimes \mathbf{t}_o \otimes \mathbf{t}_p. \tag{25}$$

The preferable anisotropy directions of the piezoelectric material are denoted as $\mathbf{t}_m$. Therefore, the components of the elasticity tensor are related by

$$C^{ijkl} = \tilde{C}^{mnop}[\bar{\mathbf{g}}^i \cdot \mathbf{t}_m][\bar{\mathbf{g}}^j \cdot \mathbf{t}_n][\bar{\mathbf{g}}^k \cdot \mathbf{t}_o][\bar{\mathbf{g}}^l \cdot \mathbf{t}_p]. \tag{26}$$

5.2 | Kinetic energy

Neglecting the contribution of rotational inertia, the kinetic energy of a Kirchhoff–Love thin shell is defined by

$$\Pi_{\text{kin}} = \frac{\rho h}{2}\int_{\Gamma}\left[\frac{\partial u_i}{\partial t}\right]^2 \mathrm{d}\Gamma, \tag{27}$$

where ρ denotes the mass density per unit volume which is here assumed constant.

5.3 | Electric enthalpy

The total electric enthalpy of the system is composed of three parts:

$$\mathfrak{E}(\mathbf{S}, \mathbf{E}) = \Pi_{\text{ela}}(\mathbf{S}) - \Pi_{\text{piezo}}(\mathbf{S}, \mathbf{E}) - \Pi_{\text{elec}}(\mathbf{E}), \tag{28}$$

where Π_{piezo} is the piezoelectric energy. The dielectric energy is denoted as Π_{elec} and the elastic energy is defined by

$$\Pi_{\text{ela}}(\mathbf{S}) = \int_{\Gamma} \tilde{W}_{\text{ela}}(\mathbf{S})\, \mathrm{d}\Gamma. \tag{29}$$

To consider the piezoelectric and the dielectric energy for a thin shell formulation, a power series expansion is applied to the electric potential with respect to the thickness coordinate ζ.[53] As the electric field is coupled to both the membrane and bending strains through the piezoelectric tensor, the first three terms are retained to thoroughly investigate the coupling effects, that is

$$\phi(\mathbf{r}(\xi, \eta, \zeta)) \approx \phi^{(0)}(\mathbf{x}(\xi, \eta)) + \zeta\phi^{(1)}(\mathbf{x}(\xi, \eta)) + \left[\zeta^2 - \left[\frac{h}{2}\right]^2\right]\phi^{(2)}(\mathbf{x}(\xi, \eta)). \tag{30}$$

The electric field is computed as

$$\mathbf{E} = -\nabla\phi, \tag{31}$$

and it can be expressed using contravariant basis vector as

$$\mathbf{E} = E_i \bar{\mathbf{g}}^i. \tag{32}$$

Due to the large relative permittivity of piezoelectric materials, the electric field in the surrounding free space is neglected. The energy contributions and hence the coupling effect depends on the configuration of the piezoelectric shell structure. Unelectroded and electroded shells along with a special short-circuited case, as displayed in Figure 5, are three options considered here.

• *Shell with no electrodes*

In this case, the shell structure is assumed to be embedded in free space, thus $\phi^{(1)} \neq 0$ and $\phi^{(2)} \neq 0$. Upon substituting expression (30), the contravariant coefficients of the electric field are calculated as

$$\begin{aligned} E_1 &= -\frac{\partial \phi}{\partial \xi} = -\phi^{(0)}_{,\xi} - \zeta \phi^{(1)}_{,\xi} - \left[\zeta^2 - \frac{h^2}{4}\right] \phi^{(2)}_{,\xi}, \\ E_2 &= -\frac{\partial \phi}{\partial \eta} = -\phi^{(0)}_{,\eta} - \zeta \phi^{(1)}_{,\eta} - \left[\zeta^2 - \frac{h^2}{4}\right] \phi^{(2)}_{,\eta}, \\ E_3 &= -\frac{\partial \phi}{\partial \zeta} = -\phi^{(1)} - 2\zeta \phi^{(2)}. \end{aligned} \tag{33}$$

The piezoelectric energy is expressed as

$$\Pi_{\text{piezo}}(\mathbf{A}, \mathbf{B}, \mathbf{E}) = \int_\Omega e^{ibc} E_i [\alpha_{bc} + \zeta \beta_{bc}] \, \mathrm{d}\Omega. \tag{34}$$

On substituting expressions (13) and (33) into (34), the piezoelectric energy can be expressed as

$$\begin{aligned} \Pi_{\text{piezo}}(\mathbf{A}, \mathbf{B}, \phi^{(0)}, \phi^{(1)}, \phi^{(2)}) = &-h \int_\Gamma e^{abc} \phi^{(0)}_{,a} \alpha_{bc} \, \mathrm{d}\Gamma - \frac{h^3}{12} \int_\Gamma e^{abc} \phi^{(1)}_{,a} \beta_{bc} \, \mathrm{d}\Gamma - h \int_\Gamma e^{3bc} \phi^{(1)} \alpha_{bc} \, \mathrm{d}\Gamma \\ &+ \frac{h^3}{6} \int_\Gamma e^{abc} \phi^{(2)}_{,a} \alpha_{bc} \, \mathrm{d}\Gamma - \frac{h^3}{6} \int_\Gamma e^{3bc} \phi^{(2)} \beta_{bc} \, \mathrm{d}\Gamma. \end{aligned} \tag{35}$$

The third-order piezoelectric tensor is expressed either in the covariant basis or the local coordinate system as

$$\mathbf{e} = e^{ijk} \bar{\mathbf{g}}_i \otimes \bar{\mathbf{g}}_j \otimes \bar{\mathbf{g}}_k = \tilde{e}^{lmn} \mathbf{t}_l \otimes \mathbf{t}_m \otimes \mathbf{t}_n, \tag{36}$$

with components related via

$$e^{ijk} = \tilde{e}^{lmn} [\bar{\mathbf{g}}^i \cdot \mathbf{t}_l][\bar{\mathbf{g}}^j \cdot \mathbf{t}_m][\bar{\mathbf{g}}^k \cdot \mathbf{t}_n]. \tag{37}$$

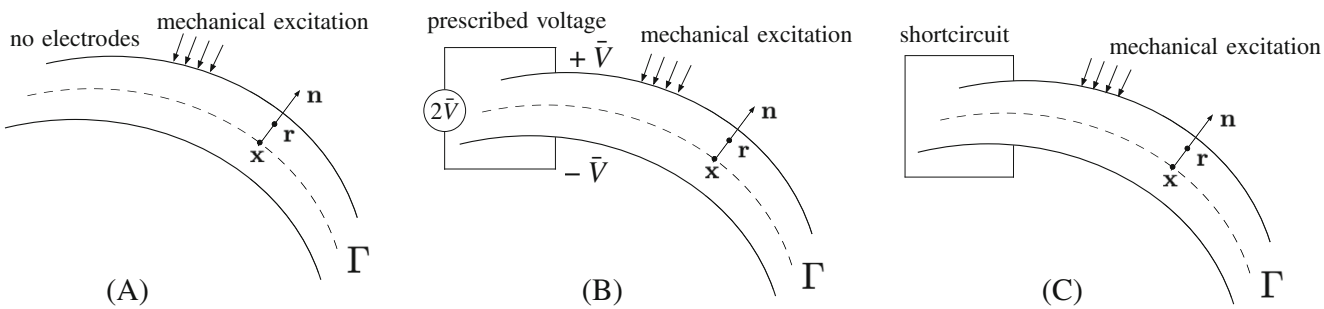

FIGURE 5 Three electric setups for piezoelectric shells. (A) A shell in free space with no electrodes. (B) An electroded shell with symmetrically prescribed voltage. (C) A special case in which the electrodes are short-circuited.

In the present work, the piezoelectric material only polarizes in the thickness direction, $\mathbf{t}_3 = \mathbf{n}$. Then, the coefficients e^{abc} can be considered as zeros. Thus two terms contribute to the piezoelectric energy, that is

$$\Pi_{\text{piezo}}(\mathbf{A}, \mathbf{B}, \phi^{(1)}, \phi^{(2)}) = -h \int_\Gamma e^{3bc}\phi^{(1)}\alpha_{bc}\, \mathrm{d}\Gamma - \frac{h^3}{6}\int_\Gamma e^{3bc}\phi^{(2)}\beta_{bc}\, \mathrm{d}\Gamma. \tag{38}$$

Because $\phi^{(0)}$ does not contribute to the piezoelectric energy, we conveniently set $\phi^{(0)} = 0$. The membrane strain is paired with the linear potential function and the bending strain is paired with the quadratic potential function. Since the electric field in the surrounding free space is neglected, the electric energy is expressed as

$$\Pi_{\text{elec}}(\phi^{(1)}, \phi^{(2)}) = \frac{h^3}{24}\int_\Gamma \kappa^{ab}\phi^{(1)}_{,a}\phi^{(1)}_{,b}\, \mathrm{d}\Gamma + \frac{h}{2}\int_\Gamma \kappa^{33}[\phi^{(1)}]^2\, \mathrm{d}\Gamma + \frac{h^5}{60}\int_\Gamma \kappa^{ab}\phi^{(2)}_{,a}\phi^{(2)}_{,b}\, \mathrm{d}\Gamma + \frac{h^3}{6}\int_\Gamma \kappa^{33}[\phi^{(2)}]^2\, \mathrm{d}\Gamma, \tag{39}$$

where the dielectric tensor is expressed in the covariant or the local coordinate systems as

$$\boldsymbol{\kappa} = \kappa^{ij}\bar{\mathbf{g}}_i \otimes \bar{\mathbf{g}}_j = \tilde{\kappa}^{kl}\mathbf{t}_k \otimes \mathbf{t}_l \tag{40}$$

with components related via

$$\kappa^{ij} = \tilde{\kappa}^{kl}[\bar{\mathbf{g}}^i \cdot \mathbf{t}_k][\bar{\mathbf{g}}^j \cdot \mathbf{t}_l]. \tag{41}$$

• *Symmetrically prescribed voltage with electrodes*

Here we assume the shell is electroded on top and bottom surface with constant voltage V_1 and V_2, respectively. Thus, as the surface potential is constant for all $\mathbf{x}$ and the following relation must be satisfied

$$\phi^{(0)} + \frac{h}{2}\phi^{(1)} = V_1, \tag{42}$$

$$\phi^{(0)} - \frac{h}{2}\phi^{(1)} = V_2. \tag{43}$$

Thus ϕ^0 and $\phi^{(1)}$ are constants and computed as

$$\phi^{(0)} = \frac{V_1 + V_2}{2}, \tag{44}$$

$$\phi^{(1)} = \frac{V_1 - V_2}{h}. \tag{45}$$

If the shell is symmetrically electroded with constant voltage, $V_1 = \bar{V}$ and $V_2 = -\bar{V}$, then $\phi^{(0)} \equiv 0$ and $\phi^{(1)} = 2\bar{V}/h$. Equation (30) thus becomes

$$\phi(\mathbf{r}(\xi, \eta, \zeta)) = \zeta\frac{2\bar{V}}{h} + \left[\zeta^2 - \left[\frac{h}{2}\right]^2\right]\phi^{(2)}(\mathbf{x}(\xi, \eta)). \tag{46}$$

Eventually, the contravariant coefficients of the electric field simplify to

$$E_1 = -\frac{\partial\phi}{\partial\xi} = -\left[\zeta^2 - \frac{h^2}{4}\right]\phi^{(2)}_{,\xi}, \quad E_2 = -\frac{\partial\phi}{\partial\eta} = -\left[\zeta^2 - \frac{h^2}{4}\right]\phi^{(2)}_{,\eta}, \quad E_3 = -\frac{\partial\phi}{\partial\zeta} = -\frac{2\bar{V}}{h} - 2\zeta\phi^{(2)}. \tag{47}$$

On substituting expressions (13) and (47) into Equation (34), the piezoelectric energy is now expressed as

$$\Pi_{\text{piezo}}(\mathbf{A}, \mathbf{B}, \phi^{(2)}) = -\frac{h^3}{6}\int_\Gamma e^{3bc}\phi^{(2)}\beta_{bc}\, \mathrm{d}\Gamma - 2\bar{V}\int_\Gamma e^{3bc}\alpha_{bc}\mathrm{d}\Gamma. \tag{48}$$

Furthermore, the electric energy can be expressed as

$$\Pi_{\text{elec}}(\phi^{(2)}) = \frac{2\bar{V}^2}{h}\kappa^{33}\int_\Gamma \mathrm{d}\Gamma + \frac{h^5}{60}\int_\Gamma \kappa^{ab}\phi^{(2)}_{,a}\phi^{(2)}_{,b}\,\mathrm{d}\Gamma + \frac{h^3}{6}\int_\Gamma \kappa^{33}[\phi^{(2)}]^2\,\mathrm{d}\Gamma. \tag{49}$$

• *Short-circuited electrodes*

A special electric condition can be obtained by short-circuiting the electrodes, thus $\bar{V} = 0$. The piezoelectric energy is now expressed as

$$\Pi_{\text{piezo}}(\mathbf{B}, \phi^{(2)}) = -\frac{h^3}{6}\int_\Gamma e^{3bc}\phi^{(2)}\beta_{bc}\,\mathrm{d}\Gamma, \tag{50}$$

while the corresponding electric energy is given by

$$\Pi_{\text{elec}}(\phi^{(2)}) = \frac{h^5}{60}\int_\Gamma \kappa^{ab}\phi^{(2)}_{,a}\phi^{(2)}_{,b}\,\mathrm{d}\Gamma + \frac{h^3}{6}\int_\Gamma \kappa^{33}[\phi^{(2)}]^2\,\mathrm{d}\Gamma. \tag{51}$$

The three electric conditions for the piezoelectric shell are summarized in Table 1.

5.4 | Stress relaxation for thin-shells

The stress tensor is denoted as $\boldsymbol{\sigma} = \sigma^{ij}\bar{\mathbf{g}}_i \otimes \bar{\mathbf{g}}_j$ with components given by

$$\sigma^{ij} = C^{ijkl}S_{kl} - e^{kij}E_k, \tag{52}$$

where S_{ij} denote the components of strain tensor $\mathbf{S}$. Since the thin shell assumption is adopted in the current work, the dominant stress components are the in-plane terms σ^{ab}. The Kirchhoff–Love assumption implies the shear stresses and strains are both neglected, thus the σ^{33} and S_{33} are the only nonzero out-of-plane components. Stress relaxation is performed by setting $\sigma^{33} = 0$, that is

$$\sigma^{33} = C^{33ij}S_{ij} - e^{i33}E_i = 0. \tag{53}$$

Since S_{i3} and S_{3j} are 0, the remaining out-of-plane strain component is computed as

$$S_{33} = -\frac{1}{C^{3333}}[C^{33ab}S_{ab} - e^{i33}E_i]. \tag{54}$$

TABLE 1 Three different electric conditions applied to the top and bottom surfaces of piezoelectric shells

	Electric functions			
Electric conditions	$\phi^{(1)}$	$\phi^{(2)}$	$\bar{V}$	**Summary**
Unelectroded	✓	✓	×	The shell is embedded in free space, the linear potential function $\phi^{(1)}$ is a variable coupled with the membrane strain. The quadratic potential function $\phi^{(2)}$ is a variable coupled with the bending strain
Prescribed voltage	×	✓	✓	The top and bottom surfaces are electroded and a constant potential difference $2\bar{V}$ is symmetrically applied between them. Thus a linear potential is prescribed which induces a global membrane strain. Only the quadratic potential function $\phi^{(2)}$ remains as a variable. If $\bar{V}$ is large, the quadratic coupling term can be ignored and the problem reduces to a one-way coupling
Short-circuited	×	✓	×	The top and bottom surfaces are electroded and short-circuited, $\bar{V} = 0$. Only the quadratic potential function $\phi^{(2)}$ is a variable

The elastic, piezoelectric and dielectric tensors are modified accordingly as

$$\hat{C}^{abcd} = C^{abcd} - \frac{C^{ab33}C^{33cd}}{C^{3333}}, \quad \hat{e}^{ijk} = e^{ijk} - \frac{e^{i33}C^{33jk}}{C^{3333}}, \quad \text{and} \quad \hat{\kappa}^{ij} = \kappa^{ij} + \frac{e^{i33}e^{j33}}{C^{3333}}. \tag{55}$$

Those modified tensors are used in the following formulation.

5.5 | External energy

The external energy contains the elastic and dielectric parts expressed as

$$\Pi_{\text{ext}}(\mathbf{u}, \phi) = \Pi_{\text{ext}}^{\text{ela}}(\mathbf{u}) + \Pi_{\text{ext}}^{\text{elec}}(\phi). \tag{56}$$

The external elastic energy is computed as

$$\Pi_{\text{ext}}^{\text{ela}}(\mathbf{u}) = h \int_{\Gamma} b_i u_i \, \mathrm{d}\Gamma + h \int_{S_t} \tau_i u_i \, \mathrm{d}S_t, \tag{57}$$

where b_i denotes the components of a body force and τ_i the components of a prescribed traction. $S_t \in \partial\Gamma$ represents the line where the traction is applied.

The external electric energy is only a function of $\phi^{(2)}$ since

$$\Pi_{\text{ext}}^{\text{elec}}(\phi^{(2)}) = \frac{h^3}{6} \int_{\Gamma} q\phi^{(2)} \, \mathrm{d}\Gamma + \frac{h^3}{6} \int_{S_d} \omega\phi^{(2)} \, \mathrm{d}S_d, \tag{58}$$

where q is the volume charge density and ω is the surface charge density on the cross-section of the shell. $S_d \in \partial\Gamma$ represents the line where the electric loads are applied. We note that the piezoelectric shell is made of a dielectric material and is thus an insulator. Since its cross-section is very thin, both volume and surface charge are difficult to apply in practical devices. The expression (58) is kept in the formulation for the sake of completeness but the contribution is neglected in the subsequent numerical examples.

5.6 | Variational setting

Hamilton's principle, ignoring dissipative mechanisms, states that the variation of the action integral of a piezoelectric shell is zero, thus

$$\delta \int_{t_0}^{t_1} L(\mathbf{u}, \psi, \varphi) \, \mathrm{d}t = 0, \tag{59}$$

where ψ and φ are henceforth used to denote $\phi^{(1)}$ and $\phi^{(2)}$ to simplify the notation. $\delta(\bullet)$ represents the variational operator and the Lagrangian is defined as

$$L(\mathbf{u}, \psi, \varphi) = \Pi_{\text{kin}}(\mathbf{u}) - \mathfrak{E}(\mathbf{u}, \psi, \varphi) + \Pi_{\text{ext}}(\mathbf{u}, \varphi). \tag{60}$$

Thus Equation (59) expands as

$$\delta \int_{t_0}^{t_1} \Pi_{\text{kin}}(\mathbf{u}) \, \mathrm{d}t - \delta \int_{t_0}^{t_1} \mathfrak{E}(\mathbf{u}, \psi, \varphi) \, \mathrm{d}t + \delta \int_{t_0}^{t_1} \Pi_{\text{ext}}(\mathbf{u}, \varphi) \, \mathrm{d}t = 0, \tag{61}$$

where the variation of the kinetic and external energy integrals can be expressed as

$$\delta \int_{t_0}^{t_1} \Pi_{\text{kin}}(\mathbf{u}) \mathrm{d}t = -\int_{t_0}^{t_1} \left[\rho h \int_{\Gamma} \delta u_i \frac{\partial^2 u_i}{\partial t^2} \, \mathrm{d}\Gamma \right] \mathrm{d}t, \tag{62}$$

and

$$\delta\int_{t_0}^{t_1}\Pi_{\text{ext}}(\mathbf{u},\varphi)\mathrm{d}t=\int_{t_0}^{t_1}\left[h\int_{\Gamma}b_i\delta u_i\,\mathrm{d}\Gamma+h\int_{S_t}t_i\delta u_i\,\mathrm{d}S_t+\frac{h^3}{6}\int_{\Gamma}q\delta\varphi\,\mathrm{d}\Gamma+\frac{h^3}{6}\int_{S_d}\omega\delta\varphi\,\mathrm{d}S_d\right]\mathrm{d}t. \tag{63}$$

The variation of the electric enthalpy for the unelectroded shell is given by

$$\begin{aligned}\delta\int_{t_0}^{t_1}\mathfrak{E}(\mathbf{u},\psi,\varphi)\,\mathrm{d}t=&\int_{t_0}^{t_1}\int_{\Gamma}h\left[\hat{C}^{abcd}\delta\alpha_{ab}\alpha_{cd}+\frac{h^2}{12}\hat{C}^{abcd}\delta\beta_{ab}\beta_{cd}\right]\,\mathrm{d}\Gamma\mathrm{d}t\\&+\int_{t_0}^{t_1}\left[h\int_{\Gamma}\hat{e}^{3bc}\psi\delta\alpha_{bc}\,\mathrm{d}\Gamma+\frac{h^3}{6}\int_{\Gamma}\hat{e}^{3bc}\varphi\delta\beta_{bc}\,\mathrm{d}\Gamma\right]\mathrm{d}t\\&+\int_{t_0}^{t_1}\left[h\int_{\Gamma}\hat{e}^{3bc}\delta\psi\alpha_{bc}\,\mathrm{d}\Gamma+\frac{h^3}{6}\int_{\Gamma}\hat{e}^{3bc}\delta\varphi\beta_{bc}\,\mathrm{d}\Gamma\right]\mathrm{d}t\\&-\int_{t_0}^{t_1}\left[\frac{h^3}{12}\int_{\Gamma}\hat{\kappa}^{ab}\delta\psi_{,a}\psi_{,b}\,\mathrm{d}\Gamma+h\int_{\Gamma}\hat{\kappa}^{33}\delta\psi\;\psi\,\mathrm{d}\Gamma\right]\mathrm{d}t\\&-\int_{t_0}^{t_1}\left[\frac{h^5}{30}\int_{\Gamma}\hat{\kappa}^{ab}\delta\varphi_{,a}\varphi_{,b}\,\mathrm{d}\Gamma+\frac{h^3}{3}\int_{\Gamma}\hat{\kappa}^{33}\delta\varphi\;\varphi\,\mathrm{d}\Gamma\right]\mathrm{d}t,\end{aligned} \tag{64}$$

and for the symmetrically electroded shell by

$$\begin{aligned}\delta\int_{t_0}^{t_1}\mathfrak{E}(\mathbf{u},\varphi)\,\mathrm{d}t=&\int_{t_0}^{t_1}\int_{\Gamma}h\left[\hat{C}^{abcd}\delta\alpha_{ab}\alpha_{cd}+\frac{h^2}{12}\hat{C}^{abcd}\delta\beta_{ab}\beta_{cd}\right]\,\mathrm{d}\Gamma\mathrm{d}t\\&+\int_{t_0}^{t_1}\left[\frac{h^3}{6}\int_{\Gamma}\hat{e}^{3bc}\varphi\delta\beta_{bc}-2\bar{V}\int_{\Gamma}\hat{e}^{3bc}\delta\alpha_{bc}\,\mathrm{d}\Gamma\right]\mathrm{d}t+\int_{t_0}^{t_1}\left[\frac{h^3}{6}\int_{\Gamma}\hat{e}^{3bc}\delta\varphi\beta_{bc}\,\mathrm{d}\Gamma\right]\mathrm{d}t\\&-\int_{t_0}^{t_1}\left[\frac{h^5}{30}\int_{\Gamma}\hat{\kappa}^{ab}\delta\varphi_{,a}\varphi_{,b}\,\mathrm{d}\Gamma+\frac{h^3}{3}\int_{\Gamma}\hat{\kappa}^{33}\delta\varphi\;\varphi\,\mathrm{d}\Gamma\right]\mathrm{d}t.\end{aligned} \tag{65}$$

To satisfy Equation (61) for all possible $\delta\mathbf{u}$, $\delta\psi$, and $\delta\varphi$ (that vanish at the end of the time interval), the weak form of the governing equation for the unelectroded shell follows as

$$\begin{aligned}&\rho h\int_{t_0}^{t_1}\int_{\Gamma}\delta u_i\frac{\partial^2u_i}{\partial t^2}\,\mathrm{d}\Gamma\mathrm{d}t\\&\quad+\int_{t_0}^{t_1}\int_{\Gamma}h\left[\hat{C}^{abcd}\delta\alpha_{ab}\alpha_{cd}+\frac{h^2}{12}\hat{C}^{abcd}\delta\beta_{ab}\beta_{cd}\right]\,\mathrm{d}\Gamma\mathrm{d}t\\&\quad+\int_{t_0}^{t_1}\left[h\int_{\Gamma}\hat{e}^{3bc}\psi\delta\alpha_{bc}\,\mathrm{d}\Gamma+\frac{h^3}{6}\int_{\Gamma}\hat{e}^{3bc}\varphi\delta\beta_{bc}\,\mathrm{d}\Gamma\right]\mathrm{d}t+\int_{t_0}^{t_1}\left[h\int_{\Gamma}\hat{e}^{3bc}\delta\psi\alpha_{bc}\,\mathrm{d}\Gamma+\frac{h^3}{6}\int_{\Gamma}\hat{e}^{3bc}\delta\varphi\beta_{bc}\,\mathrm{d}\Gamma\right]\mathrm{d}t\\&\quad-\int_{t_0}^{t_1}\left[\frac{h^3}{12}\int_{\Gamma}\hat{\kappa}^{ab}\delta\psi_{,a}\psi_{,b}\,\mathrm{d}\Gamma+h\int_{\Gamma}\hat{\kappa}^{33}\delta\psi\;\psi\,\mathrm{d}\Gamma\right]\mathrm{d}t-\int_{t_0}^{t_1}\left[\frac{h^5}{30}\int_{\Gamma}\hat{\kappa}^{ab}\delta\varphi_{,a}\varphi_{,b}\,\mathrm{d}\Gamma+\frac{h^3}{3}\int_{\Gamma}\hat{\kappa}^{33}\delta\varphi\;\varphi\,\mathrm{d}\Gamma\right]\mathrm{d}t\\&\quad+\int_{t_0}^{t_1}\left[-h\int_{\Gamma}b_i\delta u_i\,\mathrm{d}\Gamma-h\int_{S_t}\tau_i\delta u_i\,\mathrm{d}S_t-\frac{h^3}{6}\int_{\Gamma}q\delta\varphi\,\mathrm{d}\Gamma-\frac{h^3}{6}\int_{S_d}\omega\delta\varphi\,\mathrm{d}S_d\right]\mathrm{d}t\\&=0,\end{aligned} \tag{66}$$

and for the symmetrically electroded shell as

$$\begin{aligned}&\rho h\int_{t_0}^{t_1}\int_{\Gamma}\delta u_i\frac{\partial^2u_i}{\partial t^2}\,\mathrm{d}\Gamma\mathrm{d}t\\&\quad+\int_{t_0}^{t_1}\int_{\Gamma}h\left[\hat{C}^{abcd}\delta\alpha_{ab}\alpha_{cd}+\frac{h^2}{12}\hat{C}^{abcd}\delta\beta_{ab}\beta_{cd}\right]\,\mathrm{d}\Gamma\mathrm{d}t\end{aligned}$$

$$
\begin{aligned}
&+\int_{t_0}^{t_1}\left[\frac{h^3}{6}\int_\Gamma \hat{e}^{3bc}\varphi\delta\beta_{bc}-2\bar{V}\int_\Gamma \hat{e}^{3bc}\delta\alpha_{bc}\,\mathrm{d}\Gamma\right]\mathrm{d}t+\int_{t_0}^{t_1}\left[\frac{h^3}{6}\int_\Gamma \hat{e}^{3bc}\delta\varphi\beta_{bc}\,\mathrm{d}\Gamma\right]\mathrm{d}t\\
&-\int_{t_0}^{t_1}\left[\frac{h^5}{30}\int_\Gamma \hat{\kappa}^{ab}\delta\varphi_{,a}\varphi_{,b}\,\mathrm{d}\Gamma+\frac{h^3}{3}\int_\Gamma \hat{\kappa}^{33}\delta\varphi\,\varphi\,\mathrm{d}\Gamma\right]\mathrm{d}t\\
&+\int_{t_0}^{t_1}\left[-h\int_\Gamma b_i\delta u_i\,\mathrm{d}\Gamma-h\int_{S_t}\tau_i\delta u_i\,\mathrm{d}S_t-\frac{h^3}{6}\int_\Gamma q\delta\varphi\,\mathrm{d}\Gamma-\frac{h^3}{6}\int_{S_d}\omega\delta\varphi\,\mathrm{d}S_d\right]\mathrm{d}t\\
&=0.
\end{aligned}
\tag{67}
$$

5.7 | Discretization and system of equations

The displacement is discretized using the subdivision surface basis functions as

$$
\mathbf{u}=\sum_{A=0}^{n_b-1}N^A\mathbf{U}_A,
\tag{68}
$$

where n_b is the number of basis functions, and $\mathbf{U}_A$ denotes the Ath nodal coefficients of the displacement. Thus the membrane and bending strain components are computed as

$$
\alpha_{ab}=\sum_{A=0}^{n_b-1}\frac{1}{2}[N^A_{,b}\bar{\mathbf{a}}_a+N^A_{,a}\bar{\mathbf{a}}_b]\cdot\mathbf{U}_A,
\tag{69}
$$

$$
\beta_{ab}=\sum_{A=0}^{n_b-1}\left[-N^A_{,ab}\bar{\mathbf{a}}_3+\frac{1}{\bar{J}}\left[N^A_{,1}[\bar{\mathbf{a}}_{a,b}\times\bar{\mathbf{a}}_2]+N^A_{,2}[\bar{\mathbf{a}}_1\times\bar{\mathbf{a}}_{a,b}]\right]+\frac{\bar{\mathbf{a}}_3\cdot\bar{\mathbf{a}}_{a,b}}{\bar{J}}\left[N^A_{,1}[\bar{\mathbf{a}}_2\times\bar{\mathbf{a}}_3]+N^A_{,2}[\bar{\mathbf{a}}_3\times\bar{\mathbf{a}}_1]\right]\right]\cdot\mathbf{U}_A.
\tag{70}
$$

The electrical potential functions are also discretized using the same basis functions as $\mathbf{u}$, and expressed as

$$
\psi=\sum_{A=0}^{n_b-1}N^A\Psi_A,\quad \varphi=\sum_{A=0}^{n_b-1}N^A\Phi_A.
\tag{71}
$$

Here Ψ_A and Φ_A are the Ath nodal coefficients of the potential functions. Following a Bubnov–Galerkin approach, the subdivision surface bases are also used for the trial functions $\delta\mathbf{u}$ and $\delta\varphi$, and the weak form (66) follows in matrix format as

$$
\begin{bmatrix}\mathbf{M}&\mathbf{0}&\mathbf{0}\\\mathbf{0}&\mathbf{0}&\mathbf{0}\\\mathbf{0}&\mathbf{0}&\mathbf{0}\end{bmatrix}\begin{bmatrix}\ddot{\mathbf{u}}\\\mathbf{0}\\\mathbf{0}\end{bmatrix}+\begin{bmatrix}\mathbf{K}&\mathbf{C}_{u\psi}&\mathbf{C}_{u\varphi}\\\mathbf{C}_{\psi u}&\mathbf{D}_1&\mathbf{0}\\\mathbf{C}_{\varphi u}&\mathbf{0}&\mathbf{D}_2\end{bmatrix}\begin{bmatrix}\mathbf{u}\\\psi\\\varphi\end{bmatrix}=\begin{bmatrix}\mathbf{f}_u\\\mathbf{0}\\\mathbf{f}_\varphi\end{bmatrix},
\tag{72}
$$

and Equation (67) follows in matrix format as

$$
\begin{bmatrix}\mathbf{M}&\mathbf{0}\\\mathbf{0}&\mathbf{0}\end{bmatrix}\begin{bmatrix}\ddot{\mathbf{u}}\\\mathbf{0}\end{bmatrix}+\begin{bmatrix}\mathbf{K}+\mathbf{P}&\mathbf{C}_{u\varphi}\\\mathbf{C}_{\varphi u}&\mathbf{D}_2\end{bmatrix}\begin{bmatrix}\mathbf{u}\\\varphi\end{bmatrix}=\begin{bmatrix}\mathbf{f}_u\\\mathbf{f}_\varphi\end{bmatrix}.
\tag{73}
$$

Here, $\mathbf{M}$ is the global mass matrix. $\ddot{\mathbf{u}}$ is the global acceleration vector. $\mathbf{K}$ denotes the global stiffness matrix, $\mathbf{D}_1$ and $\mathbf{D}_2$ are the global dielectric system matrices, $\mathbf{C}_{u\psi}(\mathbf{C}_{u\varphi})$ and $\mathbf{C}_{\psi u}(\mathbf{C}_{\varphi u})$ are the direct and converse piezoelectric coupling matrices, respectively. The global matrix $\mathbf{P}$ has only diagonal entries and takes into account the direct piezoelectric effects caused by the prescribed voltage. $\mathbf{u}$, ψ, and φ are the global vectors of displacement, and the first and second order electrical potential coefficients, respectively. $\mathbf{f}_u$ and $\mathbf{f}_\varphi$ on the right hand side denote the global structural and electrical load vectors. Note, the system of equations is nonsymmetric. For computational efficiency, we modify the system of equations using the Schur complements $\mathbf{C}_{u\psi}\mathbf{D}_1^{-1}\mathbf{C}_{\psi u}$ and $\mathbf{C}_{u\varphi}\mathbf{D}_2^{-1}\mathbf{C}_{\varphi u}$. Thus the problem for $\mathbf{u}$ becomes

$$
\mathbf{M}\ddot{\mathbf{u}}+[\mathbf{K}-\mathbf{C}_{u\psi}\mathbf{D}_1^{-1}\mathbf{C}_{\psi u}-\mathbf{C}_{u\varphi}\mathbf{D}_2^{-1}\mathbf{C}_{\varphi u}]\mathbf{u}=\mathbf{f}_u-\mathbf{C}_{u\varphi}\mathbf{D}_2^{-1}\mathbf{f}_\varphi,
\tag{74}
$$

for the unelectroded case and

$$\mathbf{M}\ddot{\mathbf{u}} + [\mathbf{K} + \mathbf{P} - \mathbf{C}_{u\varphi}\mathbf{D}_2^{-1}\mathbf{C}_{\varphi u}]\mathbf{u} = \mathbf{f}_u - \mathbf{C}_{u\varphi}\mathbf{D}_2^{-1}\mathbf{f}_\varphi, \tag{75}$$

for shells with symmetrically prescribed voltage electrodes. Consequently, one defines new global system matrices

$$\mathbf{A} = \mathbf{K} - \mathbf{C}_{u\psi}\mathbf{D}_1^{-1}\mathbf{C}_{\psi u} - \mathbf{C}_{u\varphi}\mathbf{D}_2^{-1}\mathbf{C}_{\varphi u}, \tag{76}$$

or

$$\mathbf{A} = \mathbf{K} + \mathbf{P} - \mathbf{C}_{u\varphi}\mathbf{D}_2^{-1}\mathbf{C}_{\varphi u}, \tag{77}$$

respectively. The system of equations is thus defined by

$$\mathbf{M}\ddot{\mathbf{u}} + \mathbf{A}\mathbf{u} = \mathbf{f}_u - \mathbf{C}_{u\varphi}\mathbf{D}_2^{-1}\mathbf{f}_\varphi. \tag{78}$$

The problem of a free vibrating piezoelectric shell can be obtained by assuming harmonic motions, and is given by

$$[-\omega^2\mathbf{M} + \mathbf{A}]\mathbf{u} = \mathbf{f}_u - \mathbf{C}_{u\varphi}\mathbf{D}_2^{-1}\mathbf{f}_\varphi, \tag{79}$$

where ω is the angular frequency. For the free vibration analysis, the external mechanical and electrical loads are set to zero, and the system of equation reduces to

$$-\omega^2\mathbf{M} + \mathbf{A} = \mathbf{0}. \tag{80}$$

6 | NUMERICAL EXAMPLES

Four numerical examples are considered. This first is the free vibration of an elastic spherical thin shell which is used to validate the Kirchhoff–Love shell formulation and implementation. The electro-mechanical coupling formulation is verified by a one dimensional piezoelectric beam. Then, the piezoelectric effect for curved shells is investigated using the *Scordelis-Lo* roof geometry. The final example demonstrates the potential of the formulation by analysing the vibration of piezoelectric shell applications with complex geometry. For all the numerical examples, 2×2 Gaussian quadrature is used for regular elements and an adaptive quadrature rule[50] is used for elements with extraordinary vertices. All numerical results are computed using the open source finite element library deal.II.[54,55]

6.1 | Validation using an elastic spherical shell

The first numerical example is the free vibration analysis of an elastic spherical thin shell which is used to validate the pure elastic Kirchhoff–Love shell formulation. This problem was first examined by Lamb.[56] Baker[57] used the membrane theory to examine the axisymmetric modes of a complete spherical shell. The method developed here is based on thin shell elements and can compute both axisymmetric and nonaxisymmetric modes. Figure 6A shows cross section of the spherical shell domain Ω, which has a uniform thickness h and with Γ denoting its mid-surface. The radius R measures the distance between the center of the sphere to the mid-surface.

If the material is assumed as isotropic, the elastic strain energy density per unit area consists of the membrane and bending parts[36] as

$$\tilde{W}_{\text{ela}}(\mathbf{A}, \mathbf{B}) = \frac{1}{2}\frac{Eh}{1-\nu^2}\left[[\mathbf{A} : \mathbf{H} : \mathbf{A}] + \frac{h^2}{12}[\mathbf{B} : \mathbf{H} : \mathbf{B}]\right] = \frac{1}{2}\frac{Eh}{1-\nu^2}H^{abcd}\alpha_{ab}\alpha_{cd} + \frac{1}{2}\frac{Eh^3}{12[1-\nu^2]}H^{abcd}\beta_{ab}\beta_{cd}, \tag{81}$$

where E and ν are the Young's modulus and Poisson's ratio, respectively. H^{abcd} denote the components of the fourth-order tensor $\mathbf{H}$ computed from the contravariant metric tensors as

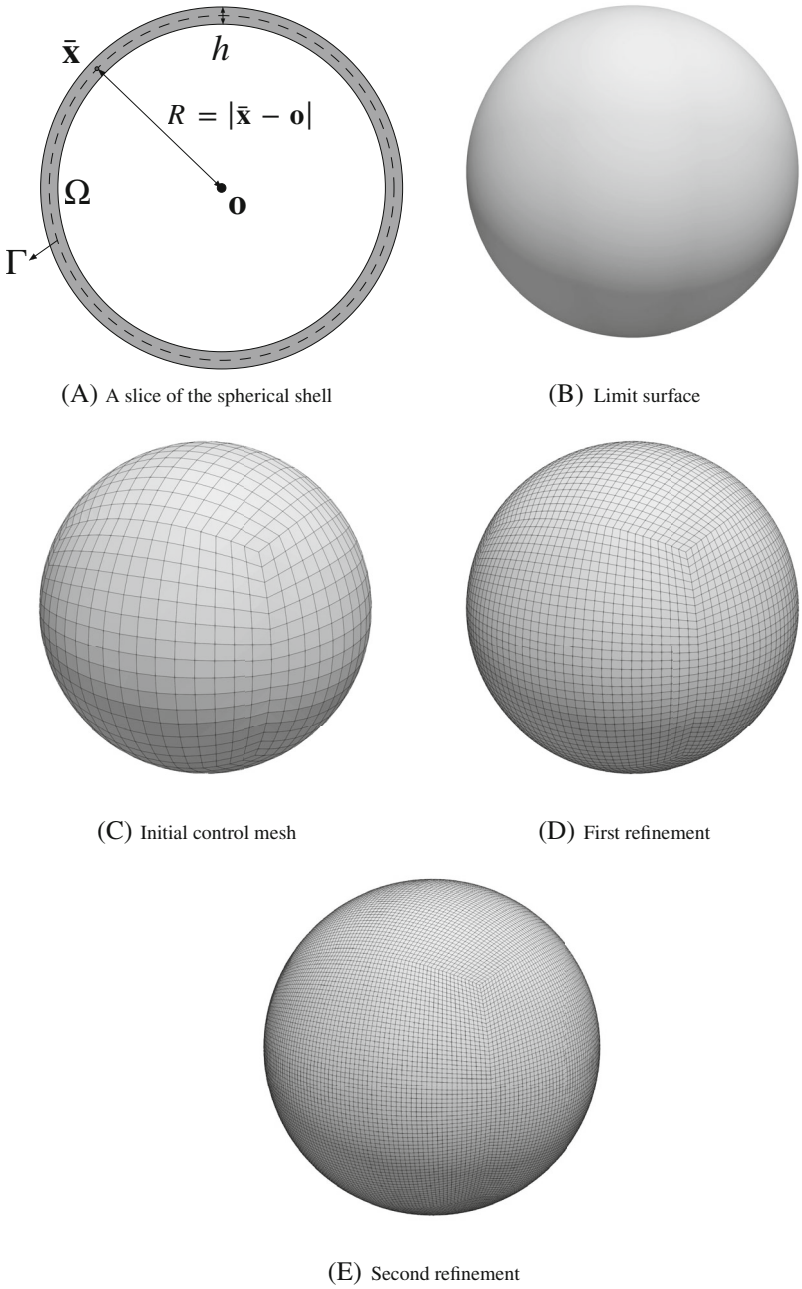

FIGURE 6 (A) Definition of a spherical shell. (B) The limiting surface constructed using Catmull–Clark subdivision from (C). (C) A control mesh with 1536 elements for the mid-surface of the spherical shell. (D) First level refined mesh with 6144 elements using a least square fitting method. (E) Second level refined mesh with 24,576 elements

$$H^{abcd} = \nu \bar{a}^{ab}\bar{a}^{cd} + \frac{1}{2}[1-\nu][\bar{a}^{ac}\bar{a}^{bd} + \bar{a}^{ad}\bar{a}^{bc}]. \tag{82}$$

Duffey et al.[58] provide a comparison of experimental results[59] with analytical solutions for the problem considered here. The values of the geometric and material parameters are given in Table 2. It is worth noting here that they used the imperial system of units in their work. Here we aim to simulate the same problem using the proposed method and compare our numerical results to experimental and analytical solutions. Since no piezoelectric effect is considered in this problem, the system of equations (80) simplifies to

$$-\omega^2 \mathbf{M} + \mathbf{K} = \boldsymbol{0}. \tag{83}$$

TABLE 2 Geometric and material parameters for the elastic spherical thin shell

Parameter	Value	
Radius R	4.4688 (in)	0.1135 (m)
Thickness h	0.0625 (in)	1.5875 (mm)
Young's modulus E	28×10^6 (psi)	193.05 (GPa)
Poisson's ratio ν	0.28	
Mass density ρ	0.000751 (lbf-s^2/in^4)	8025.937(kg/m^3)

These can be solved as an eigenvalue problem where ω^2 is the eigenvalue and the eigenvectors can be used to generate the corresponding eigenmode shapes. The natural frequency is computed as

$$f = \frac{\omega}{2\pi}. \tag{84}$$

The vibration modes of the spherical shell can be defined in terms of a polynomial degree n_d, where $n_d = 1, 2, 3, \ldots$. Each polynomial degree corresponds to a $2n_d + 1$ clustering of eigenvalues with different eigenmodes. $n_d = 1$ corresponds to a rigid body motion and the corresponding eigenvalue equals to 0. Thus the first nonzero eigenvalue corresponds $n_d = 2$. Figure 6C shows the control mesh used to construct the Catmull–Clark subdivision limit surface (Figure 6B) for the mid-surface of a spherical thin shell. The control mesh contains 1536 elements with 8 extraordinary vertices. The presence of extraordinary vertices leads to computational errors which can be reduced using an adaptive quadrature scheme.[50,60] Two refined meshes with 6144 and 24,576 elements generated using a least square fitting method are also used for this problem. Table 3 shows the numerical results for both the initial and refined control meshes. For $n_d = 2$, the numerically determined natural frequency has only a small error of approximately 0.296% for the initial mesh, 0.087% for the first level refinement and 0.024% for the second level refinement. The numerical error increases as the mode becomes more complex. For $n_d = 3$, the error is in the range of (0.180%, 0.528%) for the initial mesh and (0.062%, 0.149%) for the first level refinement and (0.021%, 0.043%) for the second level refinement. For $n_d = 4$ the errors are in the range of (0.159%, 0.510%) for the initial mesh, (0.059%, 0.147%) for the first level refinement, and (0.020%, 0.044%) for the second level refinement. The results show clear convergence to the analytical solutions and the deviation for each n_d is reduced after refinement. Figure 7 shows the vibration modes for the 1st, 6th, and 13th nonzero eigenvalues which corresponding to $n_d = 2, 3,$ and 4, respectively.

6.2 | Validation using a piezoelectric beam

The following example analyses a one-dimensional piezoelectric beam so as to validate the proposed piezoelectric Kirchhoff–Love shell formulation. Figure 8 shows the geometric configuration of the simply supported piezoelectric beam. A Lead Zirconate Titanate material PZT-H5 is chosen. This is an anisotropic crystalline piezoelectric material polarizing in the thickness direction. The geometric and material properties are shown in Table 4. The equivalent elastic modulus for the beam is computed from the fourth-order elastic tensor using the stress relaxations approach in the y and z directions. The resulting equivalent elastic modulus $\mathcal{E}_b$ is 60.39 GPa. For this choice of material and geometric properties, the analytical solution[61] of the displacements for a simply supported beam with uniform load in the absence of a piezoelectric effect, the displacement at mid-span is 2.156×10^{-4} m. The elastic stiffness of the beam will be increased by the piezoelectric effect with the effective elastic modulus[62] given by

$$\hat{\mathcal{E}}_b = \mathcal{E}_b + \frac{[e_b^{311}]^2}{\kappa_b^{33}}. \tag{85}$$

The equivalent piezoelectric coefficient can also be computed using stress relaxations, as $e_b^{311} = -16.53$ C/m^2. The equivalent dielectric coefficient $\kappa_b^{33} = 25.84 \times 10^{-9}$ C/m^2. Thus, with the 'piezoelectric stiffening effect' accounted for, the effective elastic modulus $\hat{\mathcal{E}}_b$ is enhanced to 70.97 GPa. The analytical solution of the maximum deflection $(u_z)_{\max}$ in the piezoelectric case is 1.835×10^{-4}m. The numerical test approximates this problem as the bending of a rectangular shaped

TABLE 3 Comparison of numerical results with analytical solutions and experimental results[58,59]

			Numerical results			
				f (Hz)		
n_d	Mean experimental f_e(Hz)	Analytical solutions f_a(Hz)	Nonzero eigenvalue number	Initial mesh	First refinement	Second refinement
2	5088	5078	1	5092.80	5082.37	5079.23
			2	5092.80	5082.37	5079.23
			3	5093.05	5082.41	5079.24
			4	5093.05	5082.41	5079.24
			5	5093.05	5082.41	5079.24
3	6028	6005	6	6015.79	6008.71	6006.26
			7	6015.79	6008.71	6006.26
			8	6015.79	6008.71	6006.26
			9	6025.04	6010.95	6006.81
			10	6025.04	6010.95	6006.81
			11	6025.04	6010.95	6006.81
			12	6036.72	6013.93	6007.57
4	6379	6378	13	6388.13	6381.75	6379.38
			14	6389.03	6381.94	6379.42
			15	6389.03	6381.94	6379.42
			16	6389.03	6381.94	6379.42
			17	6392.17	6382.62	6379.59
			18	6392.17	6382.62	6379.59
			19	6410.58	6387.35	6380.78
			20	6410.58	6387.35	6380.78
			21	6410.58	6387.35	6380.78

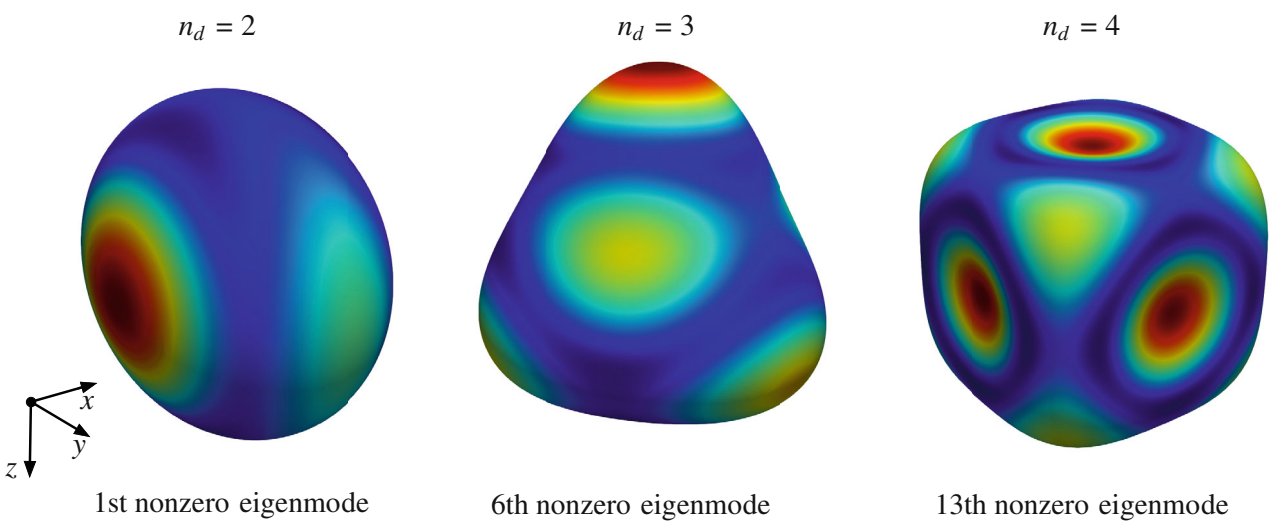

FIGURE 7 Examples of the vibration modes of the elastic spherical shell for $n_d = 2, 3,$ and 4, respectively. The color represents the magnitude of the displacement $|\mathbf{u}|$.

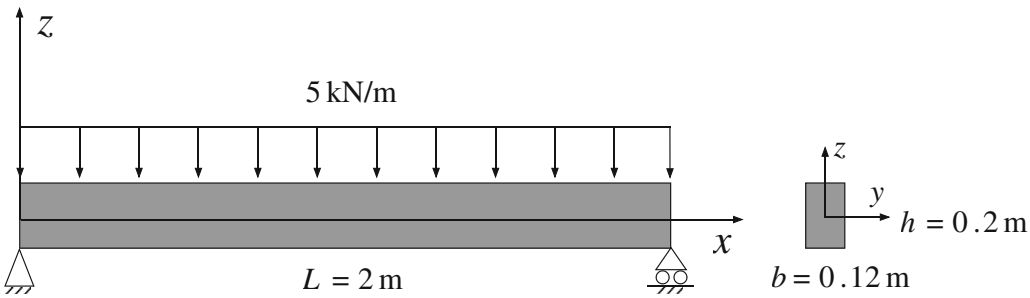

FIGURE 8 The geometric configuration of a simply supported piezoelectric beam subject to transverse mechanical loading, together with its cross-section

TABLE 4 Geometric and material parameters of the piezoelectric beam

Name	PZT-5H
Geometry	
Length L	2 m
Height (thickness) h	0.2 m
Width b	0.12 m
Material	
Elastic constants	
$\tilde{C}^{1111}, \tilde{C}^{2222}$	126 GPa
$\tilde{C}^{1122}, \tilde{C}^{2211}$	79.1 GPa
$\tilde{C}^{3333}$	117 GPa
$\tilde{C}^{1133}, \tilde{C}^{3311}, \tilde{C}^{2233}, \tilde{C}^{3322}$	83.9 GPa
$\tilde{C}^{1212}, \tilde{C}^{1221}, \tilde{C}^{2121}, \tilde{C}^{2112}$	23 GPa
Piezoelectric constants	
$\tilde{e}^{311}, \tilde{e}^{322}$	$-6.5\ \mathrm{C/m^2}$
$\tilde{e}^{333}$	$23.3\ \mathrm{C/m^2}$
Permittivity	
$\tilde{\kappa}^{11}, \tilde{\kappa}^{22}$	$15.05 \times 10^{-9}\ \mathrm{C^2/(Nm^2)}$
$\tilde{\kappa}^{33}$	$13.02 \times 10^{-9}\ \mathrm{C^2/(Nm^2)}$

shell. A coarse mesh of 10×4 elements is initially used for the numerical test and the convergence is studied using three levels of uniform refinement. Figure 9 shows the numerical prediction of the deflection and potential coefficients for the mid-surface of the beam, while Figure 10 shows that the numerical results converge to the analytical solution.

6.3 | Piezoelectric effects on the vibration of a *Scordelis-Lo* roof

The following numerical example is a *Scordelis-Lo* roof, which is commonly used as a benchmark problem for shell formulations. The *Scordelis-Lo* roof is a simple geometry which only requires a structured quadrilateral mesh without extraordinary vertices. It can be considered as a plate curved in one direction. Figure 11 shows the geometry of the roof which can be defined using a length L, a radius R and an angular parameter θ. We note here that for the well-known benchmark problem,[63] the units of the parameters are omitted. The geometry parameters are set to $L = 50$, $R = 25$ and $\theta = 40°$. The two curved edges of the roof are simply supported. The roof has a thickness $h = 0.25$ and a self-weight of 90 is applied as a uniformed load in negative z direction. The Young's modulus E for the benchmark problem is 4.32×10^8 and

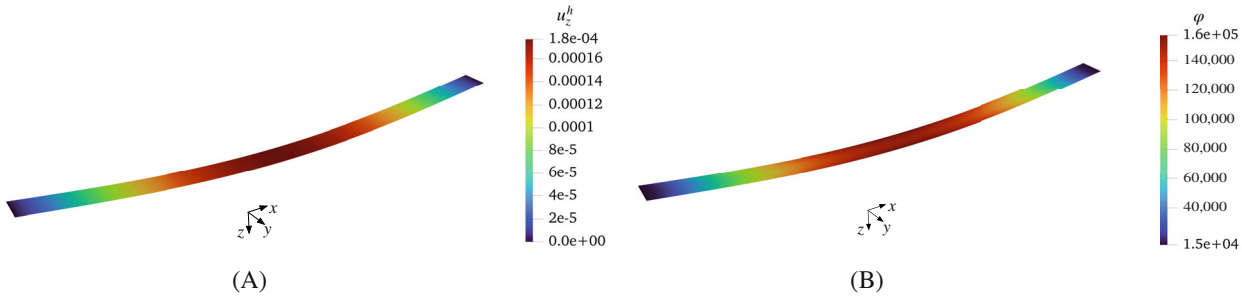

FIGURE 9 Numerical result of (A) the displacement component u_z^h and (B) the quadratic potential coefficient φ are plotted on the mid-surface of the piezoelectric beam meshed with 20×8 elements. The displacement is magnified 500 times.

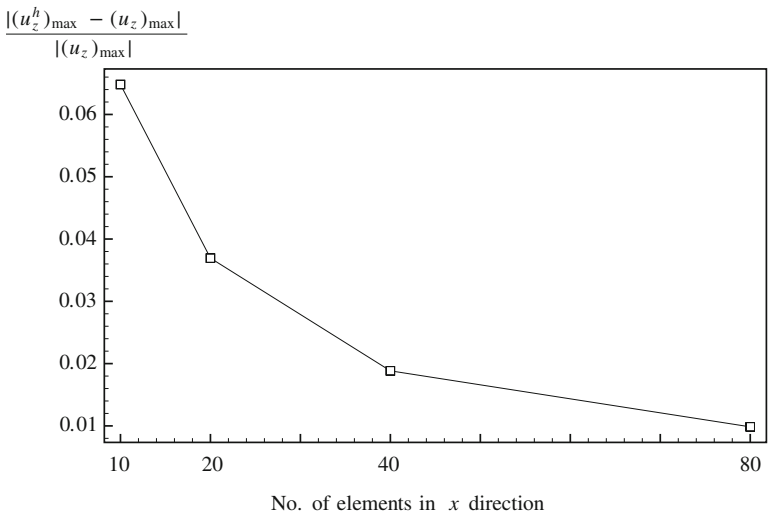

FIGURE 10 The plot of the point-wise error of the maximum deflection versus number of elements in the x-direction for the piezoelectric beam. The result converges toward the analytical solution.

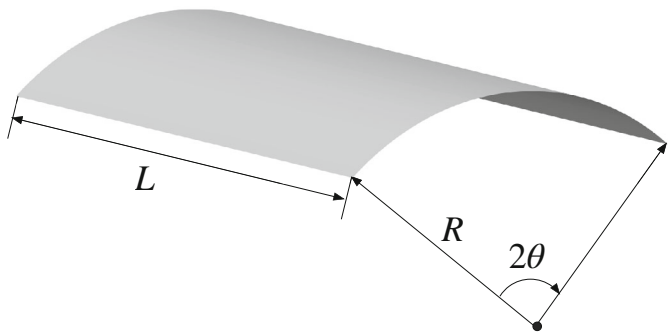

FIGURE 11 *Scordelis-Lo* roof geometry. Simply supported boundary condition are applied on the curved edges.

Poisson's ratio $\nu = 0$. The reference solution of the *Scordeli-Lo* roof shell is given by the mid-point vertical displacement u_z of the two free edges and is equal to 0.3024. Our results converge to 0.3006. Such a minor difference is also observed in other IGA shell literature.[33]

The material parameters for the piezoelectric elastic shell are also given in Table 5. The benchmark adopted an isotropic material, but the piezoelectric material considered henceforth is anisotropic. The chosen material $BaTiO_3$ has a hexagonal crystalline system with 6mm point group (Hermann–Mauguin notation).[64] The piezoelectric tensor **e** has five nonzero components when expressed in Voigt notation,[65] are $e^{31}, e^{32}, e^{33}, e^{15}$, and e^{24}. However, since the shell formulation adopts the Kirchhoff–Love and linear elastic assumptions, the components of the strain tensor S_{13}, S_{23} are zero and

TABLE 5 Geometric and material parameters of the *Scordelis-Lo* roof

Name	$BaTiO_3$
Geometry	
Length L	0.5 m
Radius R	0.25 m
Thickness h	2.5×10^{-3}m
Angle θ	$20°, 40°, 60°$
Material	
Crystalline system	Hexagonal (6 mm)
Mass density ρ	5800 kg/m^3
Elastic constants	
$\tilde{C}^{1111}, \tilde{C}^{2222}$	166 GPa
$\tilde{C}^{1122}, \tilde{C}^{2211}$	77 GPa
$\tilde{C}^{3333}$	162 GPa
$\tilde{C}^{1133}, \tilde{C}^{3311}, \tilde{C}^{2233}, \tilde{C}^{3322}$	78 GPa
$\tilde{C}^{1212}, \tilde{C}^{1221}, \tilde{C}^{2121}, \tilde{C}^{2112}$	45 GPa
Piezoelectric constants	
$\tilde{e}^{311}, \tilde{e}^{322}$	-4.4 C/m^2
$\tilde{e}^{333}$	18.6 C/m^2
Permittivity	
$\tilde{\kappa}^{11}, \tilde{\kappa}^{22}$	11.2×10^{-9} $C^2/(Nm^2)$
$\tilde{\kappa}^{33}$	12.6×10^{-9} $C^2/(Nm^2)$

stress relaxation is used to determine the elastic, piezoelectric and dielectric tensors. The only contributing components in the modified piezoelectric tensor are e^{311} and e^{322} in the ordinary tensor notation. Figure 12 shows the first 6 eigenmodes of a piezoelectric roof-like structure. The magnitude of the displacement and the electric potential functions ψ and φ distribution on the piezoelectric shell are plotted. Compared with purely elastic shells, the modal displacements do not exhibit notable change, but the coupling effect will increase the eigenmode frequencies which is known as "piezoelectric stiffening".[44] Table 6 shows the frequency increase of each eigenmode of the short-circuited and unelectroded shells. The increase is more significant for unelectroded shells due to the consideration of the additional linear potential term along the thickness direction.

The coupling effect on the piezoelectric shell with different curvature is also investigated. The arc length $L_{\text{arc}} = 2R\theta$ is held constant. Another two roof-like structure with $\theta = 20°(1/9\pi)$ and $60°(1/3\pi)$ are chosen to compare with the original *Scordelis-Lo* roof. All meshes contain 256 (16×16) elements and no extraordinary vertices. The corresponding results are also shown in Table 6. The shells with larger curvature have higher frequencies, whereby the rise in frequency is more pronounced for some eigenmodes than for others.

6.4 | Free vibration of a piezoelectric speaker

The final example considers a potential application to a piezoelectric speaker made from a single shell. The geometry considered is regenerated from a CAD model of a piezoelectric speaker. It is imported into Autodesk Maya[66] for removal of extraneous geometry. A quadrilateral control mesh for the geometry is shown in Figure 13A. A model based on Catmull–Clark subdivision surface can directly evaluate the smooth limit surface in Figure 13B using the control mesh. The limiting surface is smooth everywhere. Figure 13C,D are the top and front view of the geometry. The minimum bounding box for this model is defined by $[x_i^{\min}, x_i^{\max}]^3 = [-0.0694, 0.0694] \times [0, 0.0711] \times [-0.0694, 0.0694]\text{m}^3$. The geometry is axisymmetric about the y-axis. The thickness of the shell is 0.002 m. The eigenvalue analysis with no boundary

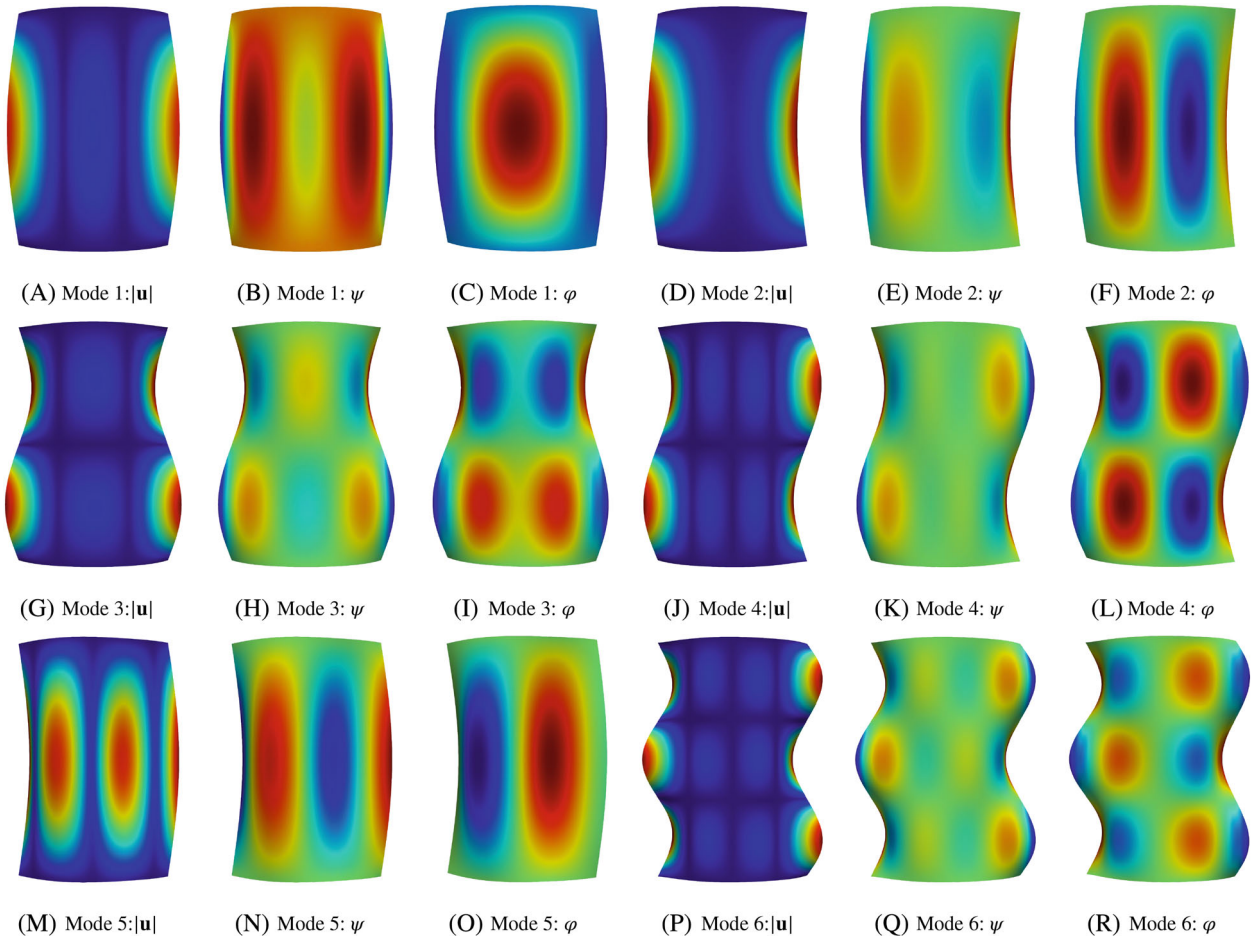

FIGURE 12 First six vibration modes of the piezoelectric *Scordeli-Lo* roof structure. The magnitude of displacements and the potential functions are plotted on the deformed mid-surface. Note, the magnitude of the displacement $|\mathbf{u}|$ is a scale in the range of $[0,|\mathbf{u}_{\max}|]$, while ψ and φ can be positive or negative. $\zeta\psi$ is the linearly varying electric potential that takes a maximum magnitude on the top and bottom surfaces of the shell, while $[\zeta^2 - h^2/4]\varphi$ is a parabolic potential function which has maximum value on the mid-surface of the shell.

constraint is performed for this example and the material $BaTiO_3$ as introduced in the previous example is chosen. The unelectroded condition is used.

Figure 14 shows the first four modes of this structure. Modes 1 and 3 are axisymmetric. Mode 2 corresponds to two identical eigenvalues which are the second and third. Similarly, mode four also relates to the fifth and sixth eigenvalues, which are also identical. Table 7 compares the eigenmode frequency of the piezoelectric shell against a pure elastic shell with approximately a 4% rise in the frequencies for the first four modes.

7 | CONCLUSIONS

An isogeometric Galerkin method for the vibration analysis of piezoelectric thin shells has been proposed. The shell formulation follows the Kirchhoff–Love hypothesis. Hamilton's variational principle has been adopted to formulate the weak form of the governing equations for the coupled problem and Catmull–Clark subdivision bases have been used for discretizing the geometry and physical fields. A Galerkin method has been implemented using the finite element library deal.II. Assuming the piezoelectric shell vibrates harmonically, the problem renders an eigenvalue problem for the system matrix. The vibration of a purely elastic shell has been verified first with a spherical shell benchmark. The piezoelectric shell formulation has also been verified with a one-dimensional beam example. Then the electromechanical coupling effects of piezoelectric shells with different curvature have been evaluated and compared using curved plates. In

TABLE 6 Eigenmode frequencies for the elastic and the piezoelectric roof-like shells with different curvatures

	$f(\theta = 20°,\ R = 50)$(Hz)			$f(\theta = 40°,\ R = 25)$(Hz)			$f(\theta = 60°,\ R = 50/3)$(Hz)		
Mode	**Elastic**	**SC**	**UE**	**Elastic**	**SC**	**UE**	**Elastic**	**SC**	**UE**
1	82.32	82.45	83.68	125.31	127.85	128.62	143.64	145.89	147.27
2	109.49	111.95	112.39	133.59	134.33	136.42	170.50	172.88	174.91
3	214.49	217.09	218.57	283.21	285.42	288.56	334.96	339.55	342.36
4	229.78	231.52	233.90	293.62	297.83	299.95	343.63	347.06	350.77
5	275.65	276.81	282.35	336.33	346.90	348.83	377.23	385.11	389.34
6	311.73	324.00	324.45	470.41	475.82	479.50	545.56	551.02	556.07
7	369.39	373.67	376.50	477.89	482.63	486.82	551.55	558.05	562.57
8	382.86	387.51	390.19	493.33	494.79	504.94	554.37	576.33	577.58

Abbreviations: SC, short-circuited shell; UE, unelectroded shell.

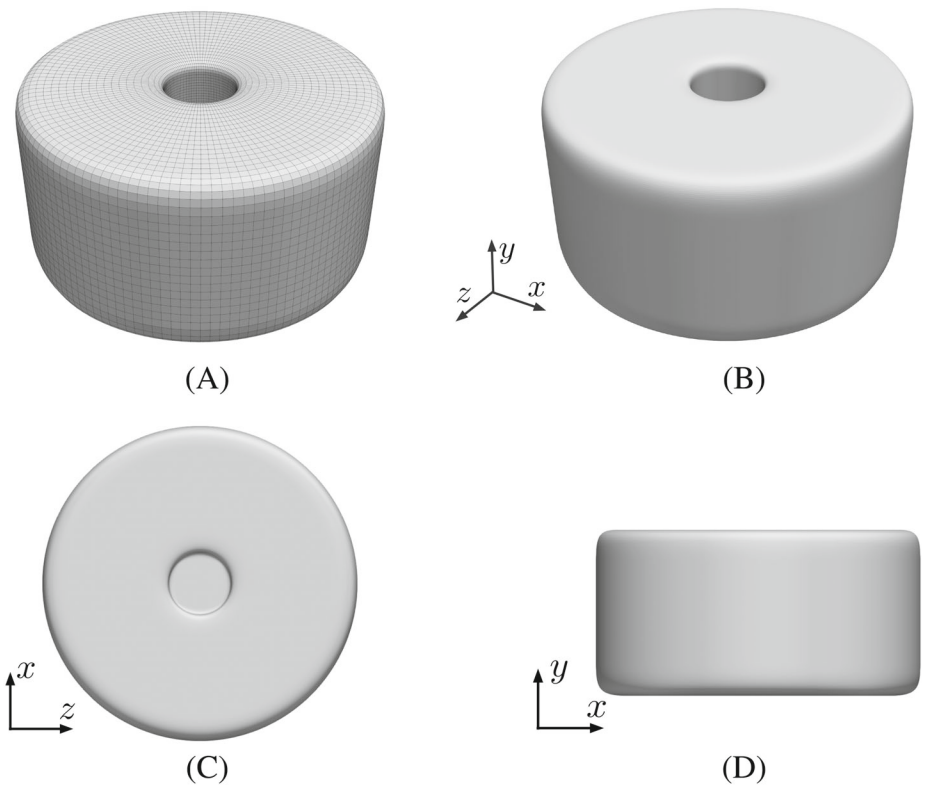

FIGURE 13 A piezoelectric buzzer geometry. (A) is a mesh of the shell with 12,288 elements. (B) is the limit subdivision surface constructed using (A). (C) is the top view of the shell and (D) represents both the front and side view of the axisymmetric geometry.

general, the natural frequencies of the piezoelectric structure are higher than those of the structure in the absence of the piezoelectric effect. This "piezoelectric stiffening" effect is particularly significant for certain modes. Finally, an example has been presented to demonstrate the capability of the proposed method in the design and analysis of piezoelectric shells with complex geometry.

The effect of piezoelectric coupling for thin shell structures with arbitrary geometries, as applicable to realistic applications generated from CAD, can clearly be described using the isogeometric method presented. It has been observed from the numerical examples that piezoelectric effect stiffens the shell structure thereby raising the natural frequency. In addition, the natural frequency of a piezoelectric shell as a function of its curvature can be accurately represented using the proposed approach. This will provide valuable guidance for the design of piezoelectric energy harvesters.

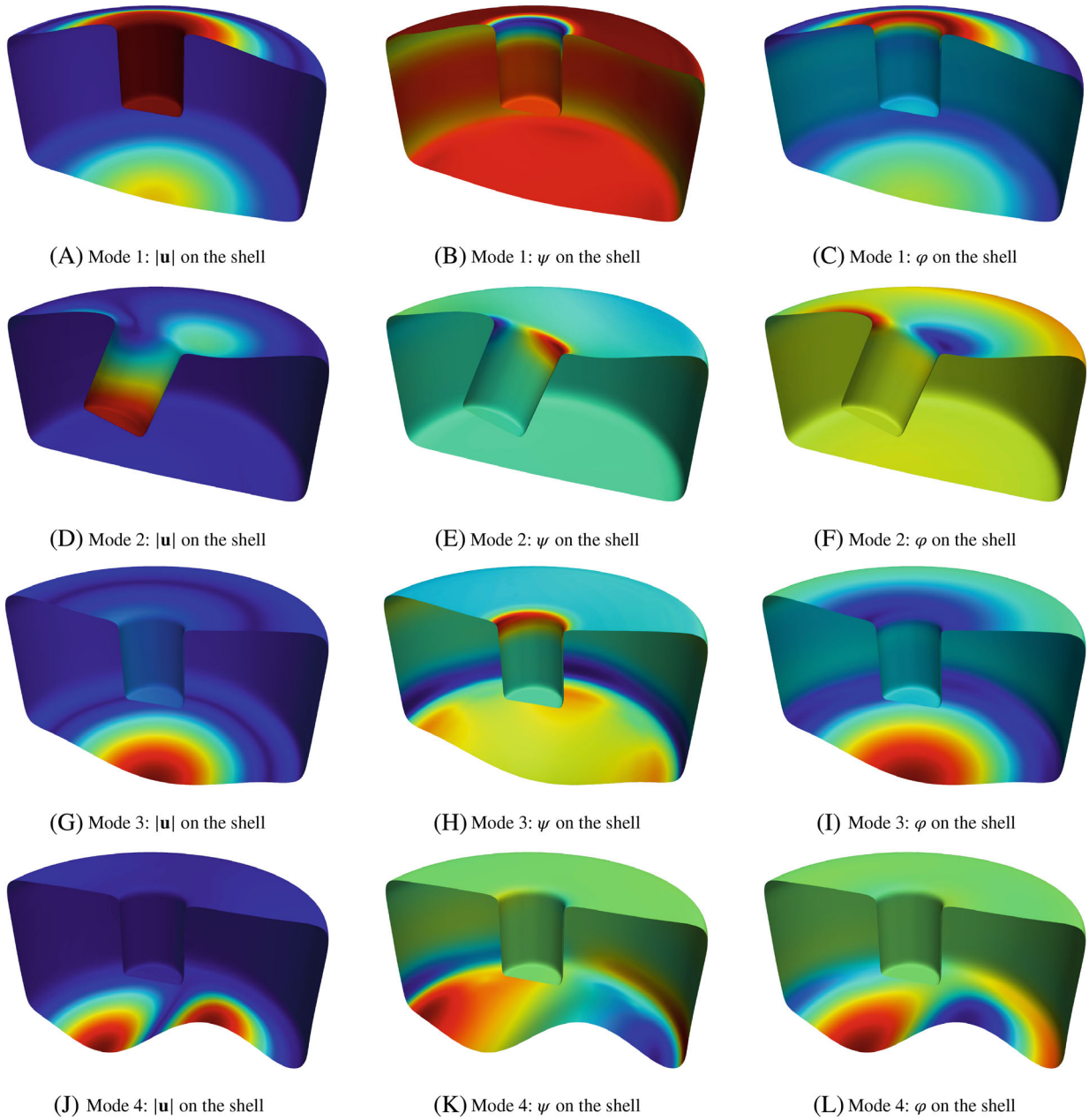

FIGURE 14 First four vibration modes of the piezoelectric speaker structure. The magnitude of displacement $|\mathbf{u}|$ and the potential functions ψ and φ are plotted on half of the deformed mid-surface of the structure. It is apparent that the linear potential function ψ is coupled to the membrane strain and that the quadratic function φ is related to bending.

TABLE 7 Eigenmode frequencies for the elastic and the piezoelectric speaker

n_d	Eigenvalue no.	Elastic f(Hz)	Coupled f(Hz)	Difference (%)
1	1	769.4	800.8	4.08
2	2,3	987.4	1032.0	4.52
3	4	1001.3	1045.5	4.41
4	5,6	1876.8	1959.0	4.38

The method allows for the straightforward incorporation of relevant electrical boundary conditions, these include no-electrodes, prescribed voltage and short-circuited. The relationship between the strain and electric potential has been made clear. For transversely isotropic piezoelectric shells polarized in the thickness direction, a linearly varying potential is generated by membrane stretching, while the bending of the shell generates a parabolic electric potential through the thickness.

In future work, the proposed method will be extended to account for large deformation and instabilities of thin shell structures made of electroelastic polymers.[67]

ACKNOWLEDGMENTS

This work was supported by the UK Engineering and Physical Sciences Research Council grant EP/R008531/1 for the Glasgow Computational Engineering Centre. We also thank for the support from the Royal Society International Exchange Scheme IES/R1/201122. Paul Steinmann gratefully acknowledges financial support for this work by the Deutsche Forschungsgemeinschaft under GRK2495, projects B & C. We are particularly grateful to Andreas Hegendörfer for discussions on the topic of piezoelectric energy harvesters. Yilin Qu also acknowledges the support from the Fundamental Research Funds for the Central Universities (No. xzy022020016).

ORCID

Zhaowei Liu https://orcid.org/0000-0002-0572-7415

REFERENCES

1. Curie J, Curie P. Piezoelectric and allied phenomena in Rochelle salt. *Comput Rend Acad Sci Paris*. 1880;91:294-297.
2. Lippmann M. On the principle of the conservation of electricity. *Lond Edinburgh Dublin Philos Mag J Sci*. 1881;12(73):151-154.
3. Curie J, Curie P. Contractions and expansions produced by voltages in hemihedral crystals with inclined faces. *Comptes Rendus*. 1881;93:1137-1140.
4. Katzir S. Who knew piezoelectricity? Rutherford and Langevin on submarine detection and the invention of sonar. *Notes Records Royal Soc*. 2012;66(2):141-157.
5. Redwood M. Transient performance of a piezoelectric transducer. *J Acoust Soc Am*. 1961;33(4):527-536.
6. Jaffe H, Berlincourt D. Piezoelectric transducer materials. *Proc IEEE*. 1965;53(10):1372-1386.
7. Abboud T, Nedéléc JC, Zhou B. Improvement of the integral equation method for high-frequency problems. Proceedings of 3rd International Conference on Mathematical Aspects of Wave Propogation Problems; 1995; SIAM Philadelphia.
8. Tzou H, Tseng C. Distributed piezoelectric sensor/actuator design for dynamic measurement/control of distributed parameter systems: a piezoelectric finite element approach. *J Sound Vib*. 1990;138(1):17-34.
9. Ng T, Liao W. Sensitivity analysis and energy harvesting for a self-powered piezoelectric sensor. *J Intell Mater Syst Struct*. 2005;16(10):785-797.
10. Safari A, Akdogan EK. *Piezoelectric and Acoustic Materials for Transducer Applications*. Springer Science & Business Media; 2008.
11. Erturk A, Inman DJ. *Piezoelectric Energy Harvesting*. John Wiley & Sons; 2011.
12. Kim HS, Kim JH, Kim J. A review of piezoelectric energy harvesting based on vibration. *Int J Precis Eng Manuf*. 2011;12(6):1129-1141.
13. Benes E, Hammer D. Piezoelectric resonator with acoustic reflectors. US Patent 4,166,967; 1979.
14. Nowotny H, Benes E. General one-dimensional treatment of the layered piezoelectric resonator with two electrodes. *J Acoust Soc Am*. 1987;82(2):513-521.
15. Hollkamp JJ. Multimodal passive vibration suppression with piezoelectric materials and resonant shunts. *J Intell Mater Syst Struct*. 1994;5(1):49-57.
16. Hagood NW, Chung WH, Von Flotow A. Modelling of piezoelectric actuator dynamics for active structural control. *J Intell Mater Syst Struct*. 1990;1(3):327-354.
17. Dosch JJ, Inman DJ, Garcia E. A self-sensing piezoelectric actuator for collocated control. *J Intell Mater Syst Struct*. 1992;3(1):166-185.
18. Hwang WS, Park HC. Finite element modeling of piezoelectric sensors and actuators. *AIAA J*. 1993;31(5):930-937.
19. Ragland K, Cullen R. Piezoelectric pressure transducer with acoustic absorbing rod. *Rev Sci Instrum*. 1967;38(6):740-742.
20. Tiersten HF, Mindlin R. Forced vibrations of piezoelectric crystal plates. *Q Appl Math*. 1962;20(2):107-119.
21. Tiersten HF. Thickness vibrations of piezoelectric plates. *J Acoust Soc Am*. 1963;35(1):53-58.
22. Nowinski J. Nonlinear transverse vibrations of orthotropic cylindrical shells. *AIAA J*. 1963;1(3):617-620.
23. Paul H. Vibrations of circular cylindrical shells of piezoelectric silver iodide crystals. *J Acoust Soc Am*. 1966;40(5):1077-1080.
24. Heyliger P. Static behavior of laminated elastic/piezoelectric plates. *AIAA J*. 1994;32(12):2481-2484.
25. Dash P, Singh B. Nonlinear free vibration of piezoelectric laminated composite plate. *Finite Elem Anal Des*. 2009;45(10):686-694.
26. Allik H, Hughes TJR. Finite element method for piezoelectric vibration. *Int J Numer Methods Eng*. 1970;2(2):151-157.
27. Benjeddou A. Advances in piezoelectric finite element modeling of adaptive structural elements: a survey. *Comput Struct*. 2000;76(1-3):347-363.

28. Ghandi K, Hagood NW. Nonlinear finite element modeling of phase transitions in electromechanically coupled material. In: Varadan VV, Chandra J, eds. *Smart Structures and Materials 1996: Mathematics and Control in Smart Structures*. Vol 2715. International Society for Optics and Photonics; 1996:121-140.
29. Lam K, Peng X, Liu G, Reddy J. A finite-element model for piezoelectric composite laminates. *Smart Mater Struct*. 1997;6(5):583.
30. Wang S. A finite element model for the static and dynamic analysis of a piezoelectric bimorph. *Int J Solids Struct*. 2004;41(15): 4075-4096.
31. Hughes TJR, Cottrell JA, Bazilevs Y. Isogeometric analysis: CAD, finite elements, NURBS, exact geometry and mesh refinement. *Comput Methods Appl Mech Eng*. 2005;194(39):4135-4195.
32. Cottrell JA, Hughes TJR, Bazilevs Y. *Isogeometric Analysis: Toward Integration of CAD and FEA*. John Wiley & Sons; 2009.
33. Kiendl J, Bletzinger KU, Linhard J, Wüchner R. Isogeometric shell analysis with Kirchhoff–Love elements. *Comput Methods Appl Mech Eng*. 2009;198(49):3902-3914.
34. Benson DJ, Bazilevs Y, Hsu MC, Hughes TJR. Isogeometric shell analysis: the Reissner–Mindlin shell. *Comput Methods Appl Mech Eng*. 2010;199(5):276-289.
35. Benson DJ, Bazilevs Y, Hsu MC, Hughes TJR. A large deformation, rotation-free, isogeometric shell. *Comput Methods Appl Mech Eng*. 2011;200(13):1367-1378.
36. Cirak F, Ortiz M, Schröder P. Subdivision surfaces: a new paradigm for thin-shell finite-element analysis. *Int J Numer Methods Eng*. 2000;47(12):2039-2072.
37. Cirak F, Ortiz M. Fully C^1-conforming subdivision elements for finite deformation thin-shell analysis. *Int J Numer Methods Eng*. 2001;51:813-833.
38. Cirak F, Ortiz M, Pandolfi A. A cohesive approach to thin-shell fracture and fragmentation. *Comput Methods Appl Mech Eng*. 2005;194(21-24):2604-2618.
39. Bandara K, Cirak F. Isogeometric shape optimisation of shell structures using multiresolution subdivision surfaces. *Comput Aided Des*. 2018;95:62-71.
40. Chen L, Lu C, Lian H, et al. Acoustic topology optimization of sound absorbing materials directly from subdivision surfaces with isogeometric boundary element methods. *Comput Methods Appl Mech Eng*. 2020;362:112806.
41. Cirak F, Deiterding R, Mauch SP. Large-scale fluid–Structure interaction simulation of viscoplastic and fracturing thin-shells subjected to shocks and detonations. *Comput Struct*. 2007;85(11-14):1049-1065.
42. Cirak F, Long Q. Subdivision shells with exact boundary control and non-manifold geometry. *Int J Numer Methods Eng*. 2011;88(9):897-923.
43. Liu Z, Majeed M, Cirak F, Simpson RN. Isogeometric FEM-BEM coupled structural-acoustic analysis of shells using subdivision surfaces. *Int J Numer Methods Eng*. 2018;113(9):1507-1530.
44. Johannsmann D. Piezoelectric stiffening. *The Quartz Crystal Microbalance in Soft Matter Research*. Springer; 2015:125-142.
45. Waisman H, Abramovich H. Active stiffening of laminated composite beams using piezoelectric actuators. *Compos Struct*. 2002;58(1):109-120.
46. Donadon M, Almeida S, De Faria A. Stiffening effects on the natural frequencies of laminated plates with piezoelectric actuators. *Compos B Eng*. 2002;33(5):335-342.
47. Stam J. Exact evaluation of Catmull-Clark subdivision surfaces at arbitrary parameter values. *SIGGRAPH Course Note*. 1998;98:395-404.
48. Peters J, Reif U. Analysis of algorithms generalizing B-spline subdivision. *SIAM J Numer Anal*. 1998;35(2):728-748.
49. Catmull E, Clark J. Recursively generated B-spline surfaces on arbitrary topological meshes. *Comput Aided Des*. 1978;10(6):350-355.
50. Liu Z, McBride A, Saxena P, Steinmann P. Assessment of an isogeometric approach with Catmull–Clark subdivision surfaces using the Laplace–Beltrami problems. *Comput Mech*. 2020;66(4):851-876.
51. Mason WP, Baerwald H. Piezoelectric crystals and their applications to ultrasonics. *Phys Today*. 1951;4(5):23.
52. Tiersten H. Hamilton's principle for linear piezoelectric media. *Proc IEEE*. 1967;55(8):1523-1524.
53. Tiersten H. Equations for the extension and flexure of relatively thin electroelastic plates undergoing large electric fields. *ASME Appl Mech Div*. 1993;161:21-21.
54. Bangerth W, Hartmann R, Kanschat G. deal.II – A general purpose object oriented finite element library. *ACM Trans Math Softw*. 2007;33(4):24/1-24/27.
55. Arndt D, Bangerth W, Davydov D, et al. The deal.II finite element library: design, features, and insights. *Comput Math Appl*. 2021;81:407-422.
56. Lamb H. On the vibrations of a spherical shell. *Proc Lond Math Soc*. 1882;1(1):50-56.
57. Baker WE. Axisymmetric modes of vibration of thin spherical shell. *J Acoust Soc Am*. 1961;33(12):1749-1758.
58. Duffey TA, Pepin JE, Robertson AN, Steinzig ML, Coleman K. Vibrations of complete spherical shells with imperfections. *J Vib Acoust*. 2007;129(3):363-370.
59. Robertson A, Hemez F, Salazar I, Duffey T. Modal testing repeatability of a population of spherical shells. No. LA-14109. Los Alamos National Lab.(LANL), Los Alamos, NM; 2004. doi: 10.2172/828954
60. Jüttler B, Mantzaflaris A, Perl R, Rumpf M. On numerical integration in isogeometric subdivision methods for PDEs on surfaces. *Comput Methods Appl Mech Eng*. 2016;302:131-146.
61. Beer FP, Johnston E, DeWolf J, Mazurek D. *Mechanics of Materials*. Springer; 1992.
62. Lurie S, Solyaev Y. On the formulation of elastic and electroelastic gradient beam theories. *Contin Mech Thermodyn*. 2019;31(6):1601-1613.

63. Belytschko T, Stolarski H, Liu WK, Carpenter N, Ong JS. Stress projection for membrane and shear locking in shell finite elements. *Comput Methods Appl Mech Eng*. 1985;51(1-3):221-258.
64. De Jong M, Chen W, Geerlings H, Asta M, Persson KA. A database to enable discovery and design of piezoelectric materials. *Sci Data*. 2015;2(1):1-13.
65. Voigt W. *Lehrbuch der kristallphysik*. Vol 962. Teubner Leipzig; 1928.
66. Autodesk, INC. Maya Version 2019.
67. Liu Z, McBride A, Sharma BL, Steinmann P, Saxena P. Coupled electro-elastic deformation and instabilities of a toroidal membrane. *J Mech Phys Solids*. 2021;151:104221.

How to cite this article: Liu Z, McBride A, Saxena P, Heltai L, Qu Y, Steinmann P. Vibration analysis of piezoelectric Kirchhoff–Love shells based on Catmull–Clark subdivision surfaces. *Int J Numer Methods Eng*. 2022;123(18):4296-4322. doi: 10.1002/nme.7010